Supporting information

Cobalt–Nickel Catalysts for Selective Hydrogenation of Carbon Dioxide into Ethanol

Lingxiang Wang[†,‡,§], Shenxian He[‡,§], Liang Wang[†,*], Ye Lei[‡], Xiangju Meng[‡], and Feng-Shou Xiao[†,‡,*]

[†]Key Lab of Biomass Chemical Engineering of Ministry of Education, College of Chemical and Biological Engineering, Zhejiang University, Hangzhou 310027, China.
[‡]Department of Chemistry, Zhejiang University, Hangzhou 310028, China.

E-mail: liangwang@zju.edu.cn; fsxiao@zju.edu.cn

[§]L. W. and S. H. contributed equally to this work.

Materials and synthesis

Materials. $Co(NO_3)_2·6H_2O$ (99.0%), $Ni(NO_3)_2·3H_2O$ (99.0%), $Al(NO_3)_3·9H_2O$ (99.0%) and $CO(NH_2)_2$ (99.5%) were obtained from Aladdin Chemical Reagent Company. $PdCl_2$ and H_2PtCl_4 were obtained from Zhejiang Metallurgical Research Institute. D_2O (D 99.9%) were supplied from Sinopharm Chemical Reagent Co., Ltd. Pure CO_2, H_2, Ar, 10% H_2/Ar, and 10% CO_2/Ar were provided by Hangzhou Jingong Special Gases Co. Ltd. D_2 were provided by Hangzhou Minxing Chemical Technology Co. Ltd.

Synthesis of $Co_{0.52}Ni_{0.48}AlO_x$ catalysts. As a typical run, the metal precursors of $Co(NO_3)_2·6H_2O$ (30 mmol), $Ni(NO_3)_2·3H_2O$ (30 mmol) and $Al(NO_3)_3·9H_2O$ (20 mmol) were dissolved in 200 mL deionized water, followed by the addition of 600 mmol of $CO(NH_2)_2$. After stirring the mixture at 105 °C for 8 h, the precipitate was separated by filtration, washed with deionized water, and dried at 100 °C for overnight to obtain the $Co_{0.52}Ni_{0.48}$Al-LDH. The $Co_{0.52}Ni_{0.48}$Al-oxides was obtained by calcining the $Co_{0.52}Ni_{0.48}$Al-LDH at 400 °C for 4 h. After reducing the $Co_{0.52}Ni_{0.48}$Al-oxides in flowing hydrogen (10% H_2/Ar, 60 mL/min) for 3 h at different temperatures, the $Co_{0.52}Ni_{0.48}AlO_x$-*T* catalyst was obtained, where *T* is the reduction temperature (*T* = 300, 400, 500, 600, or 650 °C). The Co/Ni ratio for $Co_{0.52}Ni_{0.48}AlO_x$-600 was 52/48 by inductively coupled plasma (ICP) analysis. If there is no special note, the $Co_{0.52}Ni_{0.48}AlO_x$ is the catalyst reduced in hydrogen at 600 °C.

Synthesis of $Co_mNi_nAlO_x$ catalysts with different Co/Ni ratios. $Co_mNi_nAlO_x$ catalysts with different Co/Ni ratios at 67/33 and 20/80 were synthesized following the similar synthesis procedures to $Co_{0.52}Ni_{0.48}AlO_x$ except for changing the initial amount of $Co(NO_3)_2·6H_2O$ and $Ni(NO_3)_2·3H_2O$ to 40 mmol and 20 mmol for $Co_{0.67}Ni_{0.33}AlO_x$, and 20 mmol and 40 mmol for $Co_{0.20}Ni_{0.80}AlO_x$, respectively. If there is no special note, the $Co_{0.67}Ni_{0.33}AlO_x$ and $Co_{0.20}Ni_{0.80}AlO_x$ are the catalysts reduced in hydrogen at 600 °C.

Synthesis of $CoAlO_x$ and $NiAlO_x$ catalysts. $CoAlO_x$ and $NiAlO_x$ catalysts were synthesized from the similar synthesis procedures to $Co_{0.52}Ni_{0.48}AlO_x$ except changing the metal precursors. Apart from same amount of $Al(NO_3)_3·9H_2O$, either 60 mmol of $Co(NO_3)_2·6H_2O$ or $Ni(NO_3)_2·3H_2O$ were used in the synthesis of $CoAlO_x$ and $NiAlO_x$ catalysts, respectively. If there is no special note, the $CoAlO_x$ and $NiAlO_x$ are the catalysts reduced with hydrogen at 600 °C.

Synthesis of $Pd_{0.05}/CoAlO_x$ and $Pt_{0.05}/CoAlO_x$ catalysts. As a typical run, the metal precursors of $Co(NO_3)_2·6H_2O$ (30 mmol), $Al(NO_3)_3·9H_2O$ (10 mmol) and 30 mL of $PdCl_2$ (0.05 $mol·L^{-1}$) aqueous solution were mixed in 200 mL of deionized water, followed by the addition of 300 mmol of $CO(NH_2)_2$. After stirring the mixture at 105 °C for 8 h, the precipitate was separated by filtration, washed with deionized water, and dried at 100 °C for overnight to obtain the $Co_{0.95}Pd_{0.05}$Al-LDH. The $Co_{0.95}Pd_{0.05}$Al-oxides was obtained by calcining the $Co_{0.95}Pd_{0.05}$Al-LDH at 400 °C for 4 h. After reducing $Co_{0.95}Pd_{0.05}$Al-oxides in flowing hydrogen (10% H_2/Ar, 60 mL/min) for 3 h at 600 °C, the $Pd_{0.05}/CoAlO_x$ catalyst was obtained. $Pt_{0.05}/CoAlO_x$ catalyst was synthesized from the abovementioned procedures except using H_2PtCl_4 (0.05 $mol·L^{-1}$) rather than $PdCl_2$ (0.05 $mol·L^{-1}$) aqueous solution.

Characterization

X-ray diffraction (XRD) patterns were collected on a Rigaku D/MAX 2550 diffract meter with Cu Kα radiation (λ= 1.5406 Å). The composition of catalysts were measured with an inductively coupled plasma (ICP) analysis (Perkin-Elmer 3300DV). H_2-temperature programmed reduction (H_2-TPR) was performed on a Finesorb-3010. X-ray photoelectron spectra (XPS) of the samples were recorded using a Kratos AXIS Supra with Al Kα X-ray radiations as the X-ray source. The binding energies were calibrated on the basis of C 1s (284.8 eV) peak. The Co L-edges and Ni L-edges soft X-ray absorption spectra (XAS) were measured at the BL12B-a beamline of the National Synchrotron Radiation Laboratory (NSRL). Scanning electron microscopy (SEM) were performed on a Hitachi SU-1510 electron microscopy. Transmission electron microscopy (TEM) and scanning transmission electron microscopy (STEM) images were obtained on a JEM-2100F electron microscopy with an acceleration voltage of 200 kV. Mass spectra (MS) were recorded on a GCMS-QP2010 mass spectrometry. ^{1}H NMR spectra and ^{1}H COSY NMR spectra were recorded on an Agilent DD2 600 spectrometer at resonance frequency of 600 MHz.

In-situ FT-IR characterization. IR spectra were recorded using a Thermo Fisher Nicolet iS50 FT-IR spectrometer equipped with an MCT/A detector and ZnSe window, and a high temperature reaction chamber. As a typical run, 50 mg of solid sample was localized in the chamber and pretreated at 200 °C for 30 min in flowing Ar (20 mL/min). Then, the chamber was adjusted to desired temperature (250 °C), and CO_2 (10% CO_2 in Ar) was flowed to the sample for 30 min. After removing the physically adsorbed CO_2 by pure Ar gas, the FT-IR spectra of CO_2 adsorbed on the samples were recorded (Figure S24).

In order to observe the transformation of reaction intermediates on the catalyst surface, H_2 (10% H_2 in Ar) was pulsed into the chamber after the catalyst was pretreated with CO_2, the FT-IR spectra of reaction intermediates adsorbed on the samples were recorded (Figures 1a, 4a, S26, S27 and S31). In addition, the intensity of IR peaks was analyzed (Figures 1b, 4b–d, S30 and S32).

In-situ Raman characterization. Raman spectra were recorded using a HR800 Raman spectrometer equipped with an Ar excitation source (λ=514.532 nm). The hydrogen was introduced into the sample chamber (10% H_2 in Ar) to reduce the solid sample at desired temperatures for 20 min, then the spectra were collected (Figures S14 and S15). In order to investigate the CO_2 adsorption on the samples, CO_2 was introduced into the chamber after the reduction pretreatment, then the spectra were collected. For further studying the reaction on the samples, the abovementioned procedures were repeated except using mixed gas of CO_2 and H_2 (1:3) in the treatment (Figures S28 and S29).

Catalyst evaluation

The CO_2 hydrogenation was carried out in a stainless-steel reactor with Teflon inner container. As a typical run, 25 mg of catalyst and 2 mL of H_2O were mixed into the reactor. The reactor was sealed and flushed five times with 1.0 MPa of CO_2 to remove the air, then the CO_2/H_2 gas mixture was charged in to 4.0 MPa (H_2/CO_2 = 3:1), and the autoclave was heated to desired temperature in an oil bath. The temperature was

measured by a thermocouple in the oil bath. After reaction, the reactor was cooled in the mixture of ice and water. The composition of gas in the autoclave was analyzed with a Fu Li-9790 gas phase chromatography (GC) equipped with thermal conductivity detector (TCD). The liquor was separated from the solid catalyst by centrifugation and analyzed by a Shimadzu GC-2014 chromatograph equipped with flame ionization detector (FID) with benzyl alcohol as internal standard. In the recycle tests, the solid catalyst was separated by centrifugation, washed with deionized water, dried at 80 °C for 2 h, and then used in the next run. The product yield and selectivity are based on the moles of carbon. The CO hydrogenation was performed under the equivalent conditions except using CO instead of CO_2 in the reactor.

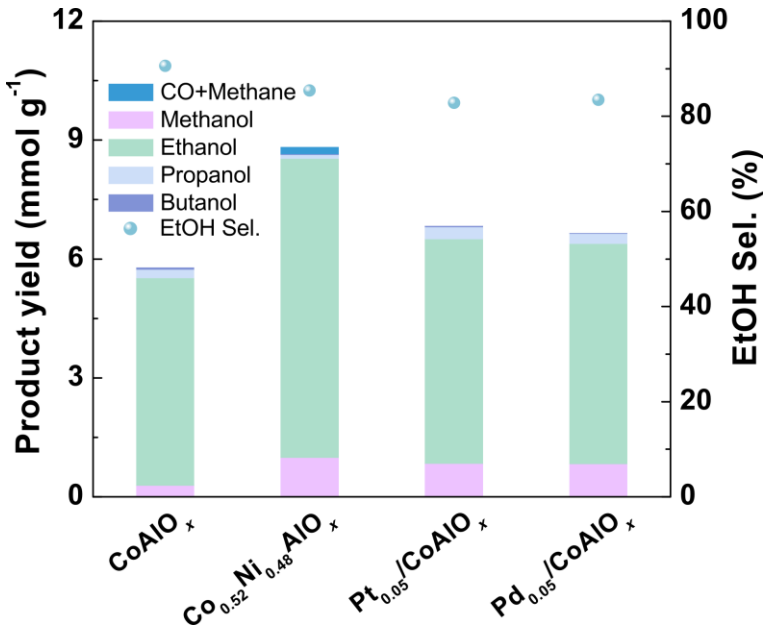

Figure S1. Catalytic performance of various catalysts in CO_2 hydrogenation. Reaction conditions: catalyst (25 mg), H_2O (2 mL), initial pressure 4.0 MPa (H_2/CO_2 = 3:1), 12 h, 140 °C. The yield and selectivity are based on the number of moles of carbon.

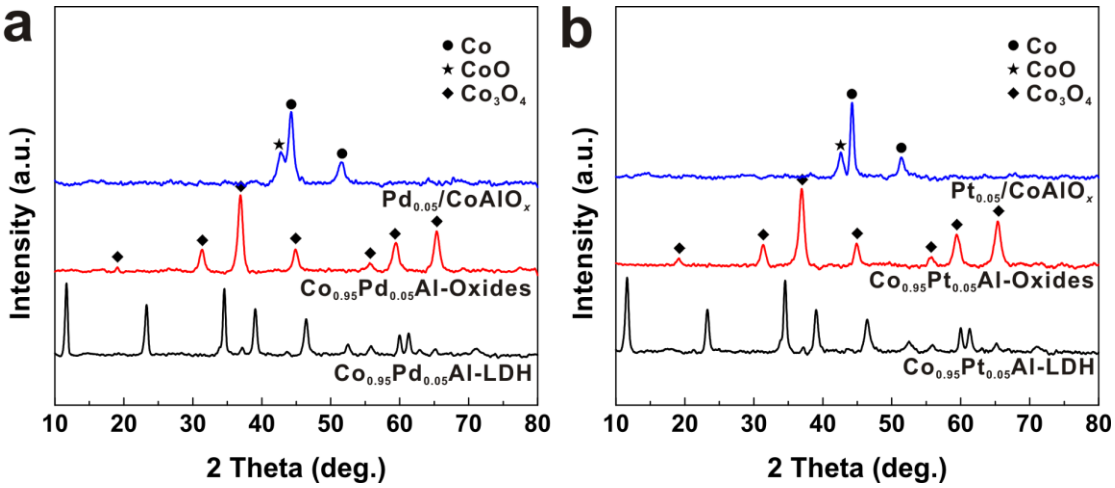

Figure S2. XRD patterns of (a) $Co_{0.95}Pd_{0.05}$Al-LDH, $Co_{0.95}Pd_{0.05}$Al-oxides, and $Pd_{0.05}/CoAlO_x$ catalyst, and (b) $Co_{0.95}Pt_{0.05}$Al-LDH, $Co_{0.95}Pt_{0.05}$Al-oxides, and $Pt_{0.05}/CoAlO_x$ catalyst.

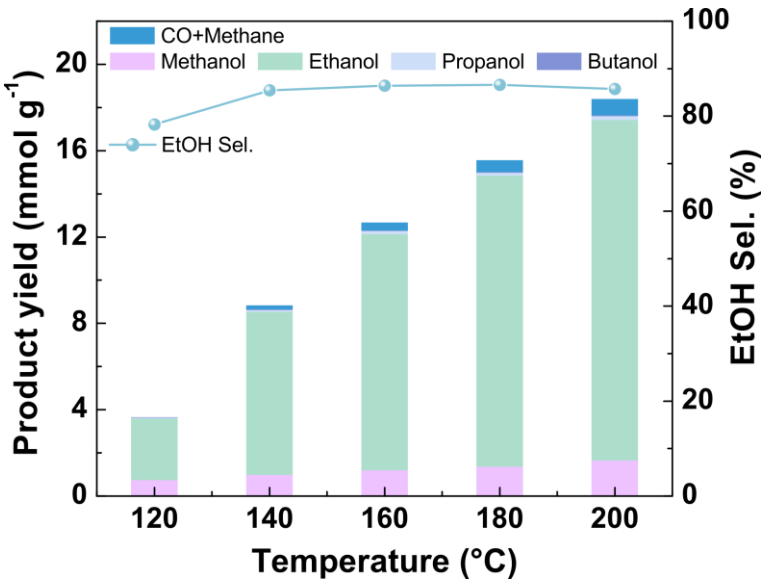

Figure S3. Dependences of product yield and ethanol selectivity on temperature over the $Co_{0.52}Ni_{0.48}AlO_x$ catalyst. Reaction conditions: catalyst (25 mg), H_2O (2 mL), initial pressure 4.0 MPa (H_2/CO_2 = 3:1), 12 h. The yield and selectivity are based on the number of moles of carbon.

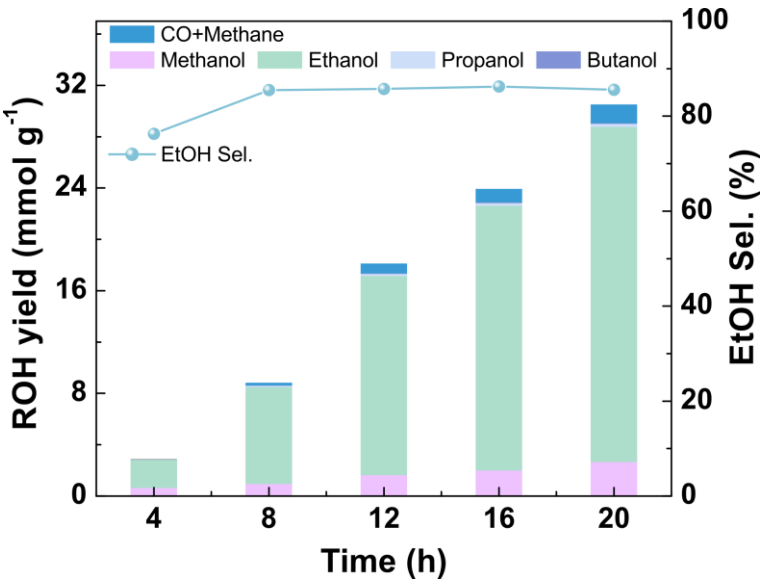

Figure S4. Dependences of product yield and ethanol selectivity on time over the $Co_{0.52}Ni_{0.48}AlO_x$ catalyst. Reaction conditions: catalyst (25 mg), H_2O (2 mL), initial pressure 4.0 MPa (H_2/CO_2 = 3:1), 12 h. The yield and selectivity are based on the number of moles of carbon.

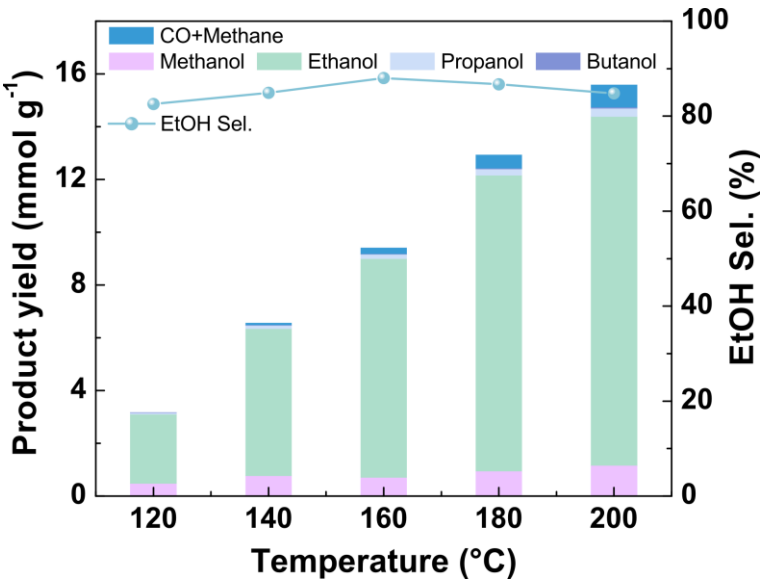

Figure S5. Dependences of product yield and ethanol selectivity on temperature over the $Co_{0.67}Ni_{0.33}AlO_x$ catalyst. Reaction conditions: catalyst (25 mg), H_2O (2 mL), initial pressure 4.0 MPa (H_2/CO_2 = 3:1), 12 h. The yield and selectivity are based on the number of moles of carbon.

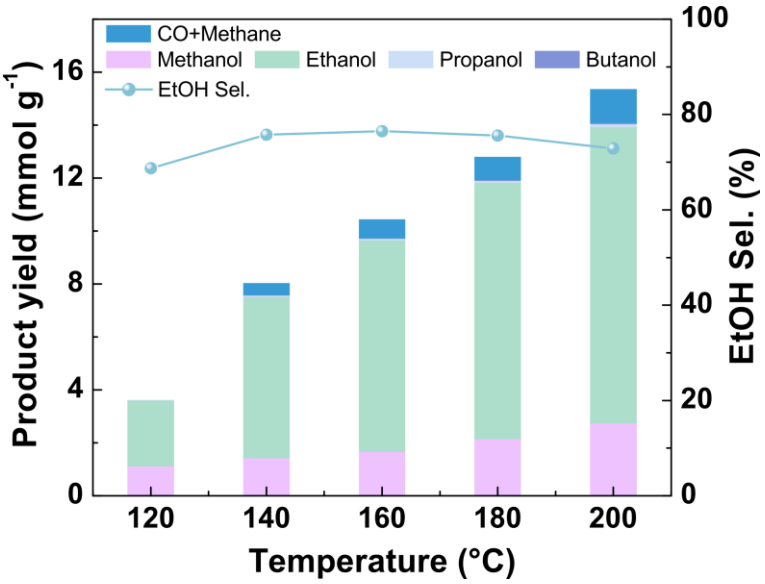

Figure S6. Dependences of product yield and ethanol selectivity on temperature over the $Co_{0.20}Ni_{0.80}AlO_x$ catalyst. Reaction conditions: catalyst (25 mg), H_2O (2 mL), initial pressure 4.0 MPa (H_2/CO_2 = 3:1), 12 h. The yield and selectivity are based on the number of moles of carbon.

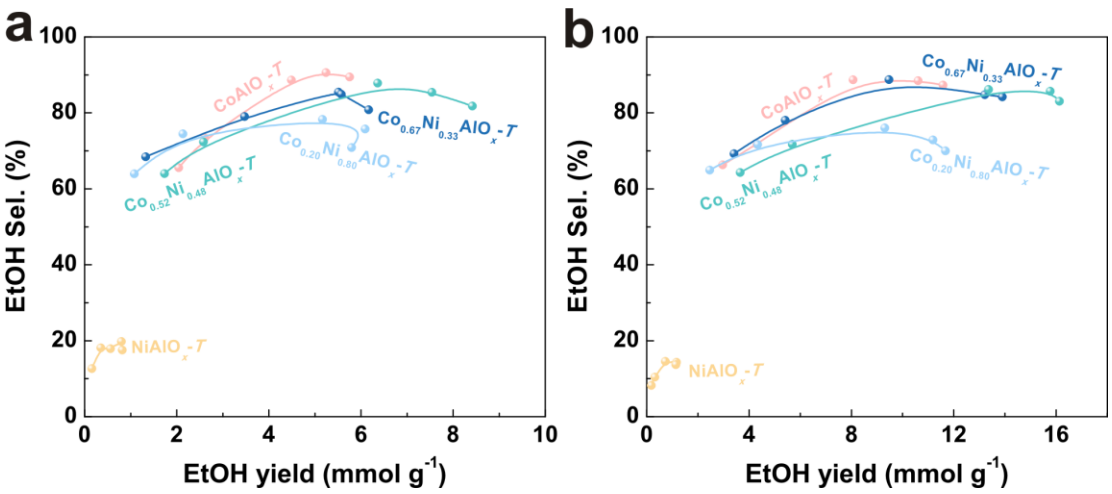

Figure S7. Dependences of ethanol selectivity on yield over various $Co_mNi_nAlO_x$-*T* catalysts obtained under different reduction temperature. Reaction conditions: catalyst (25 mg), H_2O (2 mL), initial pressure 4.0 MPa (H_2/CO_2 = 3:1), 12 h, (a) 140 °C and (b) 200 °C. The yield and selectivity are based on the number of moles of carbon.

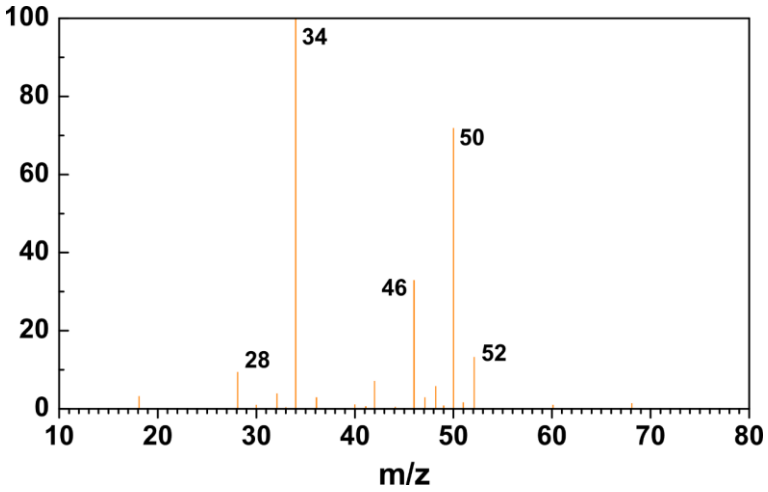

Figure S8. Mass spectrum of C_2D_5OD from CO_2 hydrogenation with D_2 over $Co_{0.52}Ni_{0.48}AlO_x$ catalyst.

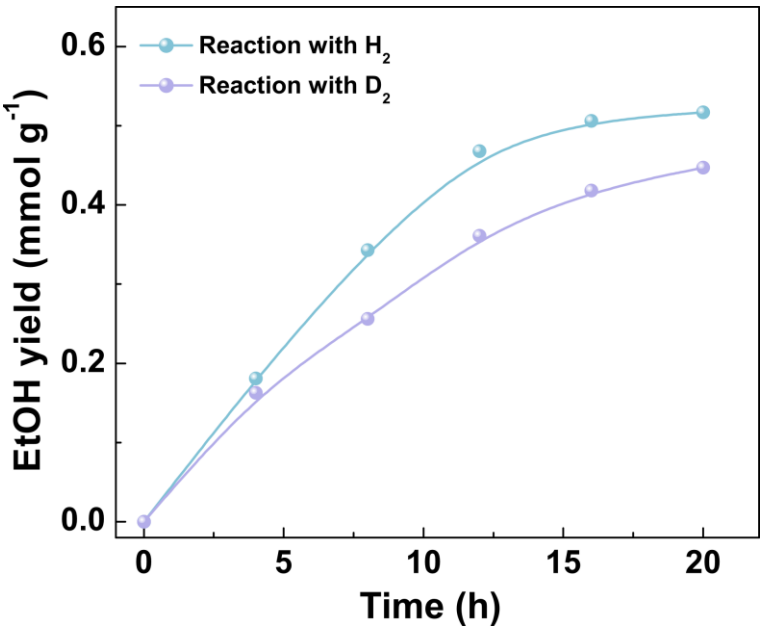

Figure S9. Kinetic isotopic effects on ethanol yield from CO_2 hydrogenation over $Co_{0.52}Ni_{0.48}AlO_x$ catalyst. Reaction conditions: catalyst (25 mg), H_2O (2 mL), initial pressure (2.0 MPa, H_2 or D_2/CO_2 = 3:1). The yield and selectivity are based on the number of moles of carbon.

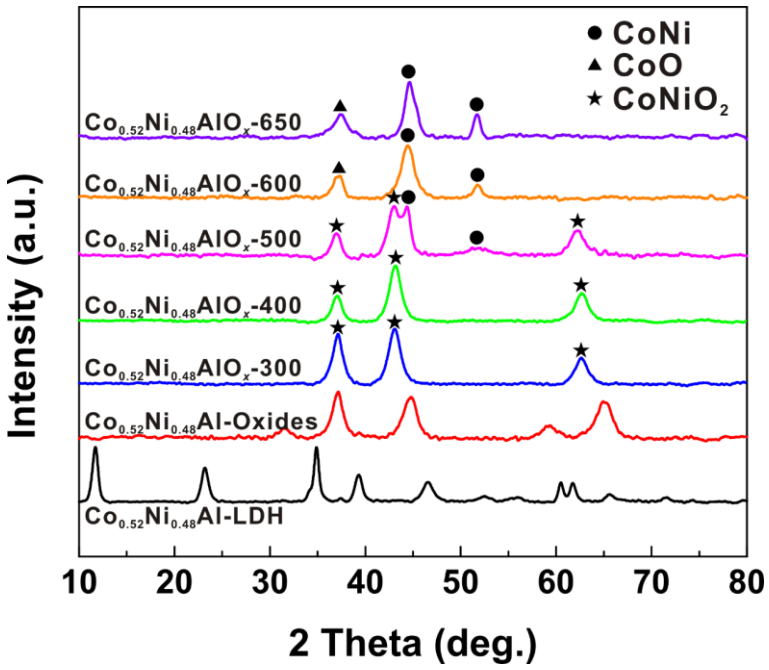

Figure S10. XRD patterns of $Co_{0.52}Ni_{0.48}$Al-LDH, $Co_{0.52}Ni_{0.48}$Al-oxides, and $Co_{0.52}Ni_{0.48}AlO_x$-*T* catalysts obtained at different reduction temperatures.

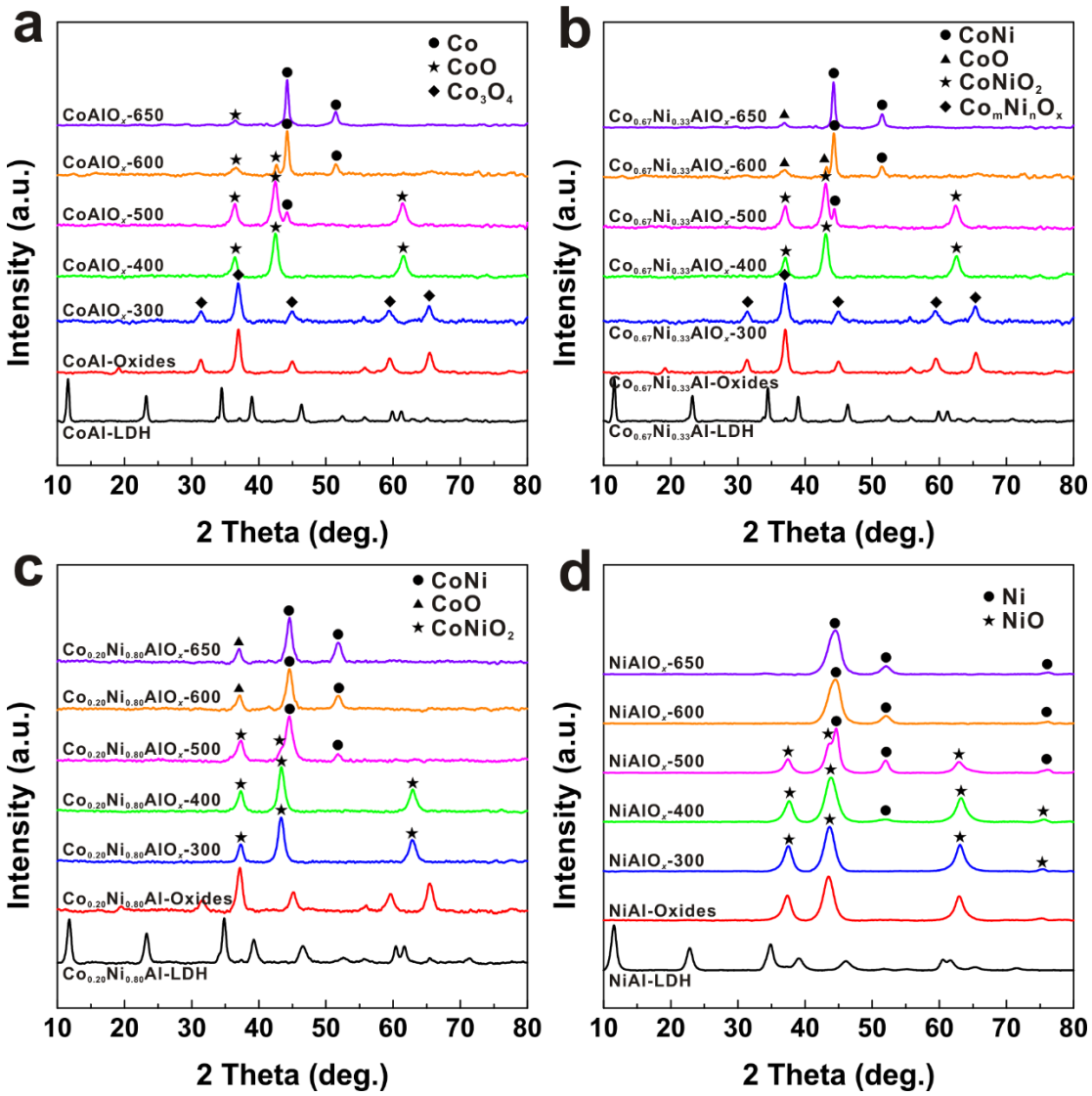

Figure S11. XRD patterns of Co_mNi_nAl-LDH, Co_mNi_nAl-oxides, and $Co_mNi_nAlO_x$-*T* catalysts obtained at different reduction temperatures.

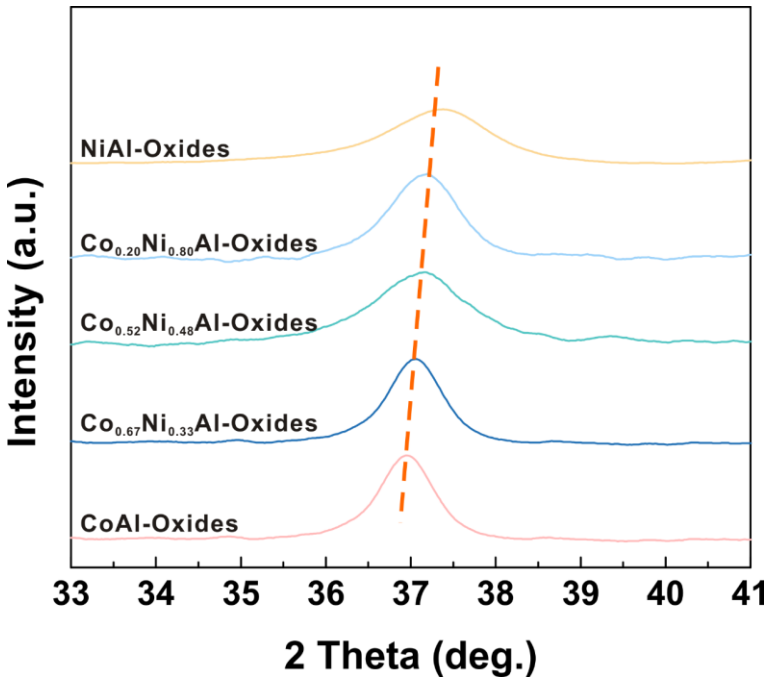

Figure S12. Expanded XRD patterns of Co_mNi_nAl-oxides with various Co/Ni ratios.

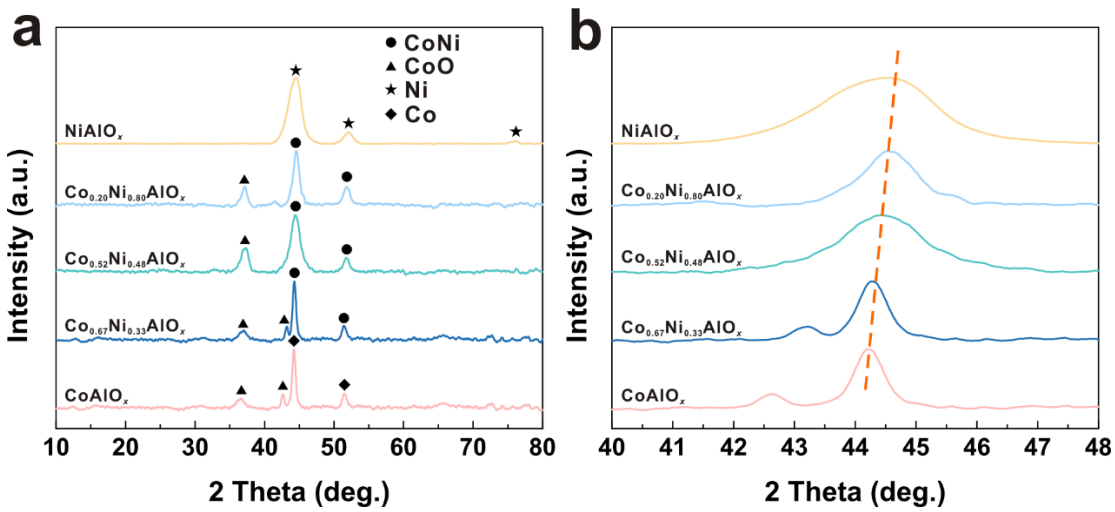

Figure S13. (a) XRD patterns and (b) expanded XRD patterns of $Co_mNi_nAlO_x$ catalysts with various Co/Ni ratios.

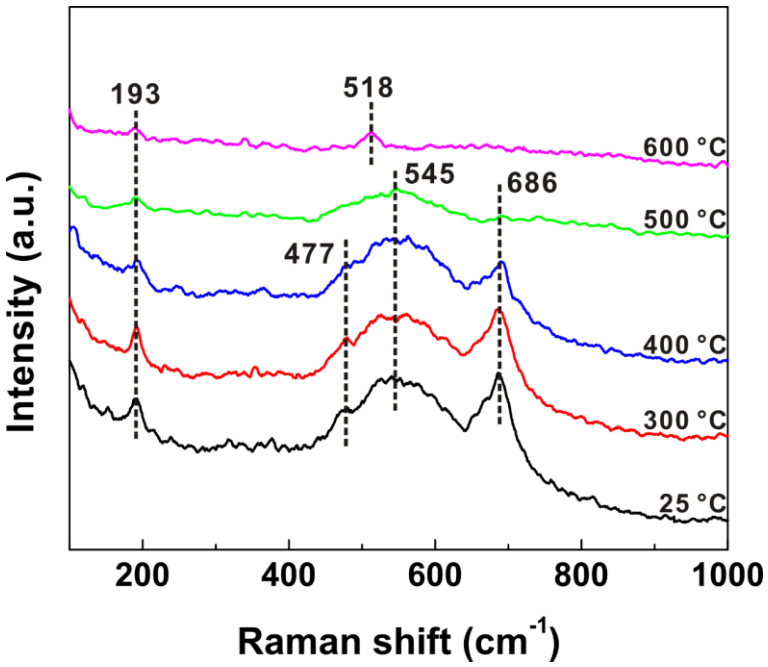

Figure S14. *In-situ* Raman spectra of $Co_{0.52}Ni_{0.48}Al$-oxides under H_2 reduction treatment.

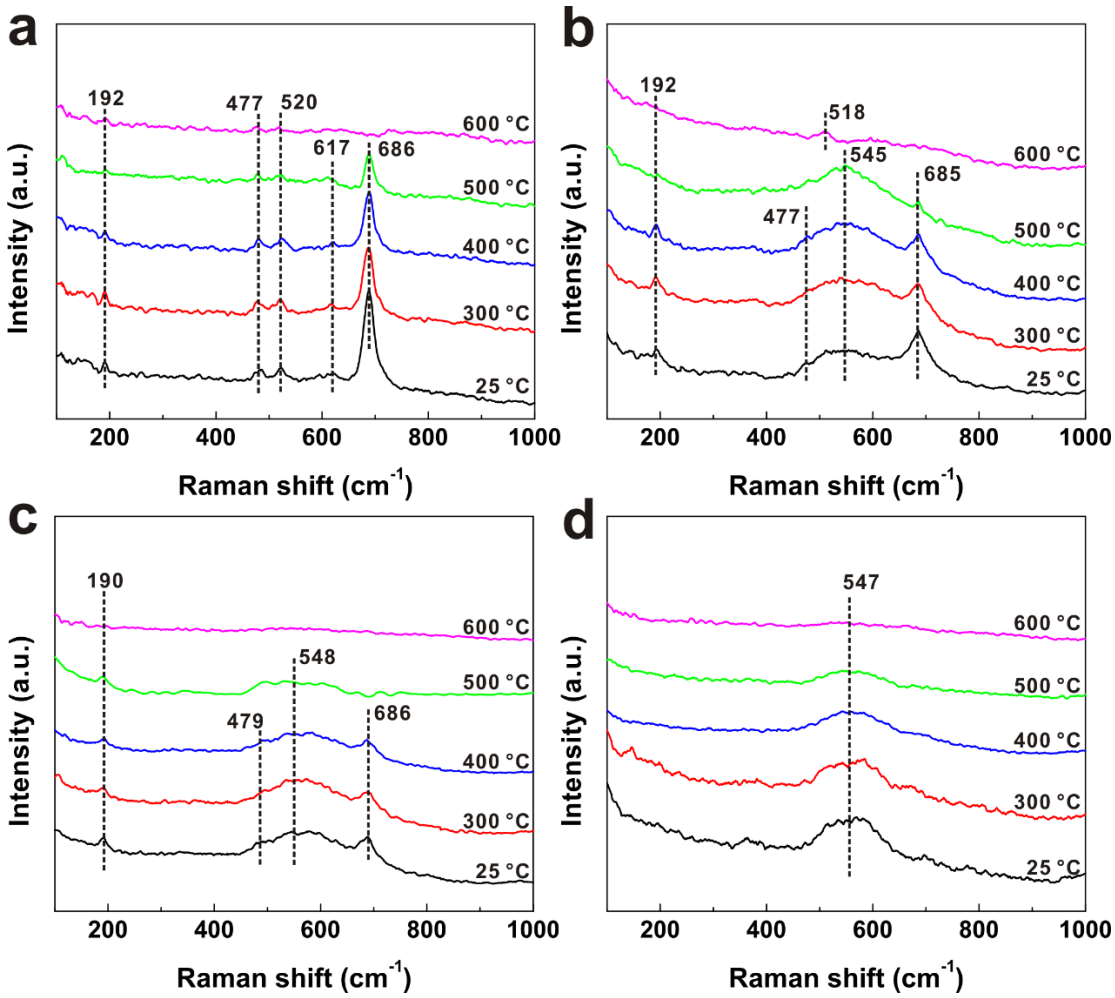

Figure S15. *In-situ* Raman spectra of (a) CoAl-oxides, (b) $Co_{0.67}Ni_{0.33}$Al-oxides, (c) $Co_{0.20}Ni_{0.80}$Al-oxides and (d) NiAl-oxides under H_2 reduction treatment.

Note: The $Co_{0.67}Ni_{0.33}AlO_x$ shows similar reaction trend to $Co_{0.52}Ni_{0.48}AlO_x$ catalyst, giving metallic CoNi alloy and unreduced CoO species after reduction at 600 °C. In contrast, the $Co_{0.20}Ni_{0.80}AlO_x$ with more nickel species give the CoNi alloy with almost undetectable of CoO.

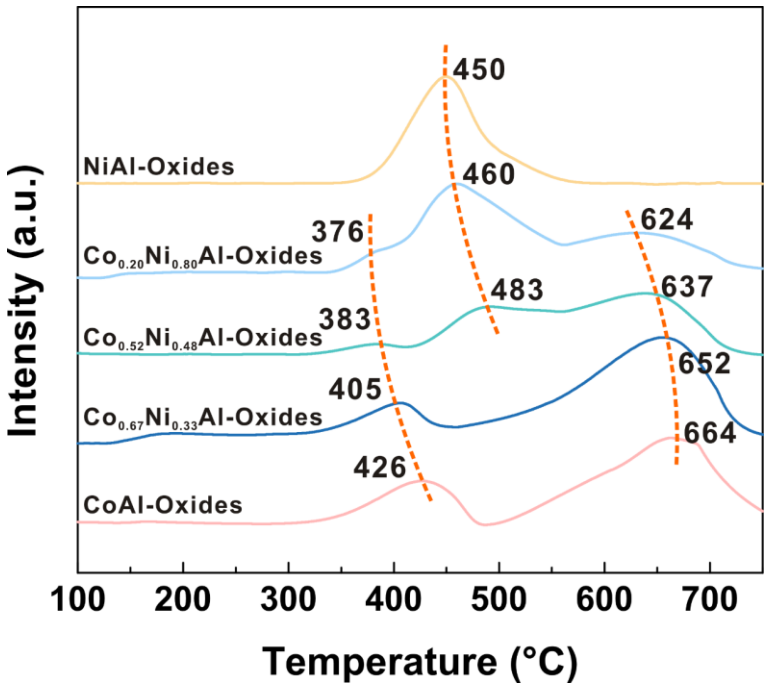

Figure S16. H_2-TPR profiles of $Co_mNi_nAlO_x$ catalysts with various Co/Ni ratios.

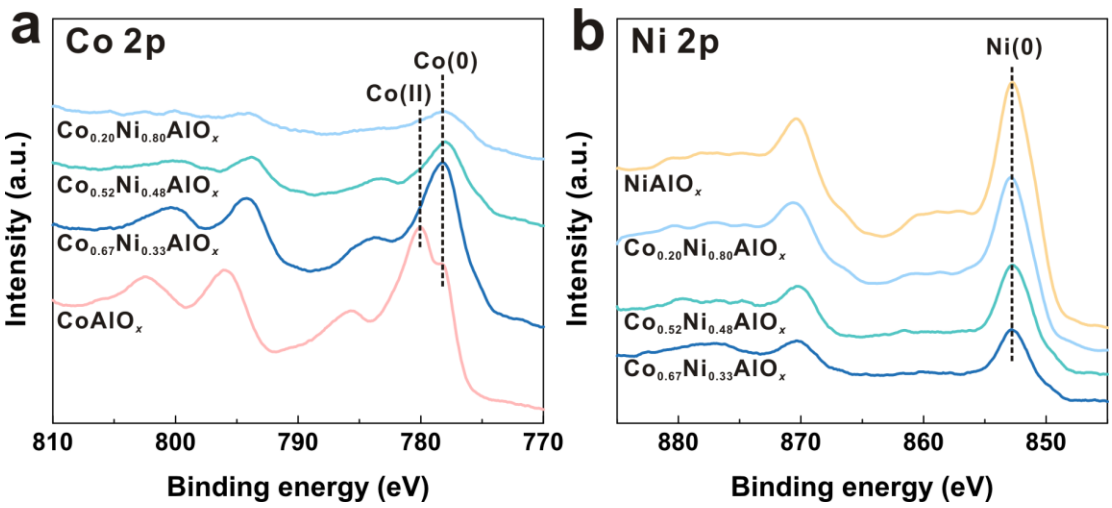

Figure S17. Co 2p and Ni 2p XPS spectra of $Co_mNi_nAlO_x$ catalysts.

Note: $Co_mNi_nAlO_x$ catalysts show obvious peaks at 778.0 and 780.0 eV in Co 2p XPS spectra, assigned to the Co^0 and Co^{2+} species. Ni 2p XPS spectra exhibit peaks at 852.7 eV attributed to the Ni^0 species on the sample. These Co and Ni signals might originate from the metallic CoNi alloy and CoO species on the reduced catalysts.

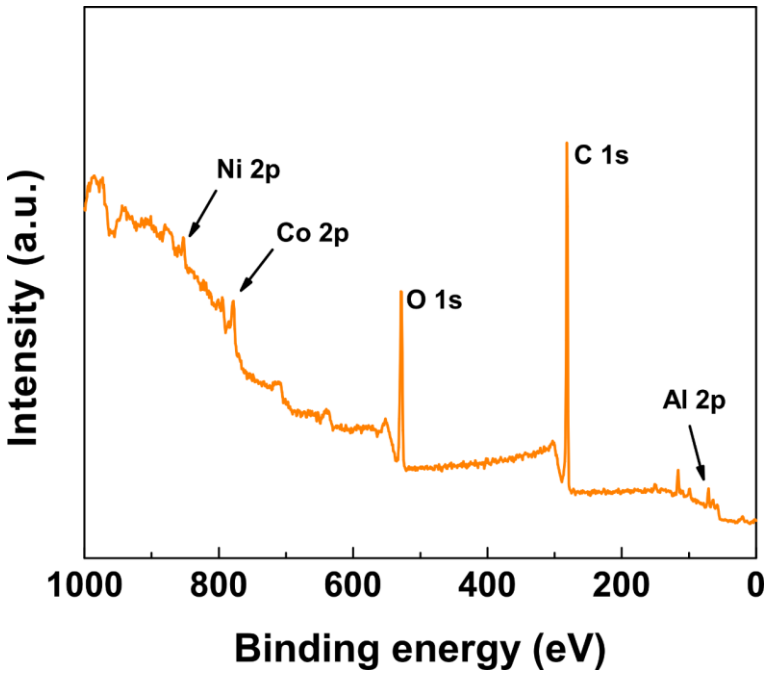

Figure S18. XPS full spectrum of $Co_{0.52}Ni_{0.48}AlO_x$ catalyst.

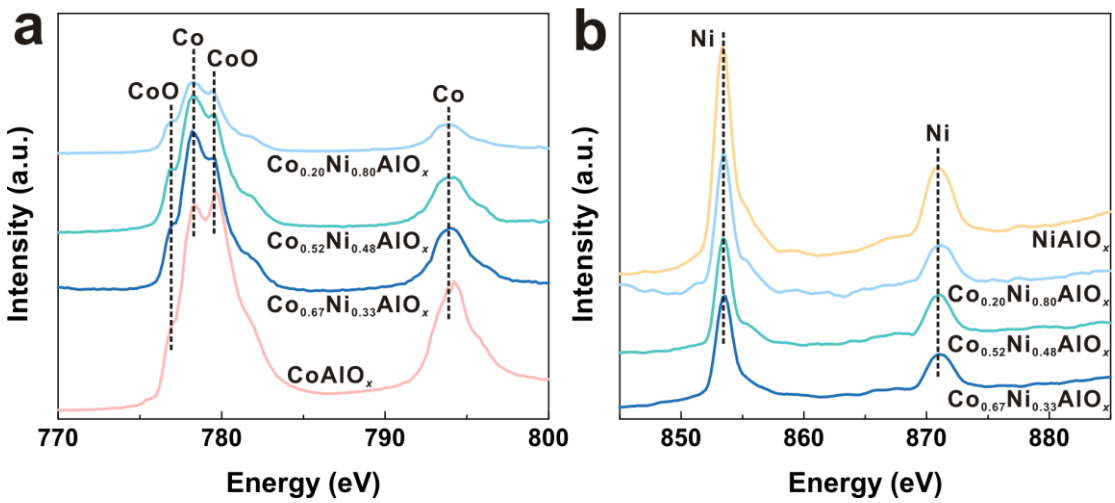

Figure S19. XAS of (a) Co L-edges and (b) Ni L-edges for various samples.

Note: The signals of CoO, metallic Co, and metallic Ni are observed on the Co and Ni L-edges, which should be from the CoO and metallic CoNi phases, in good agreement with the XPS results (Figure S17).

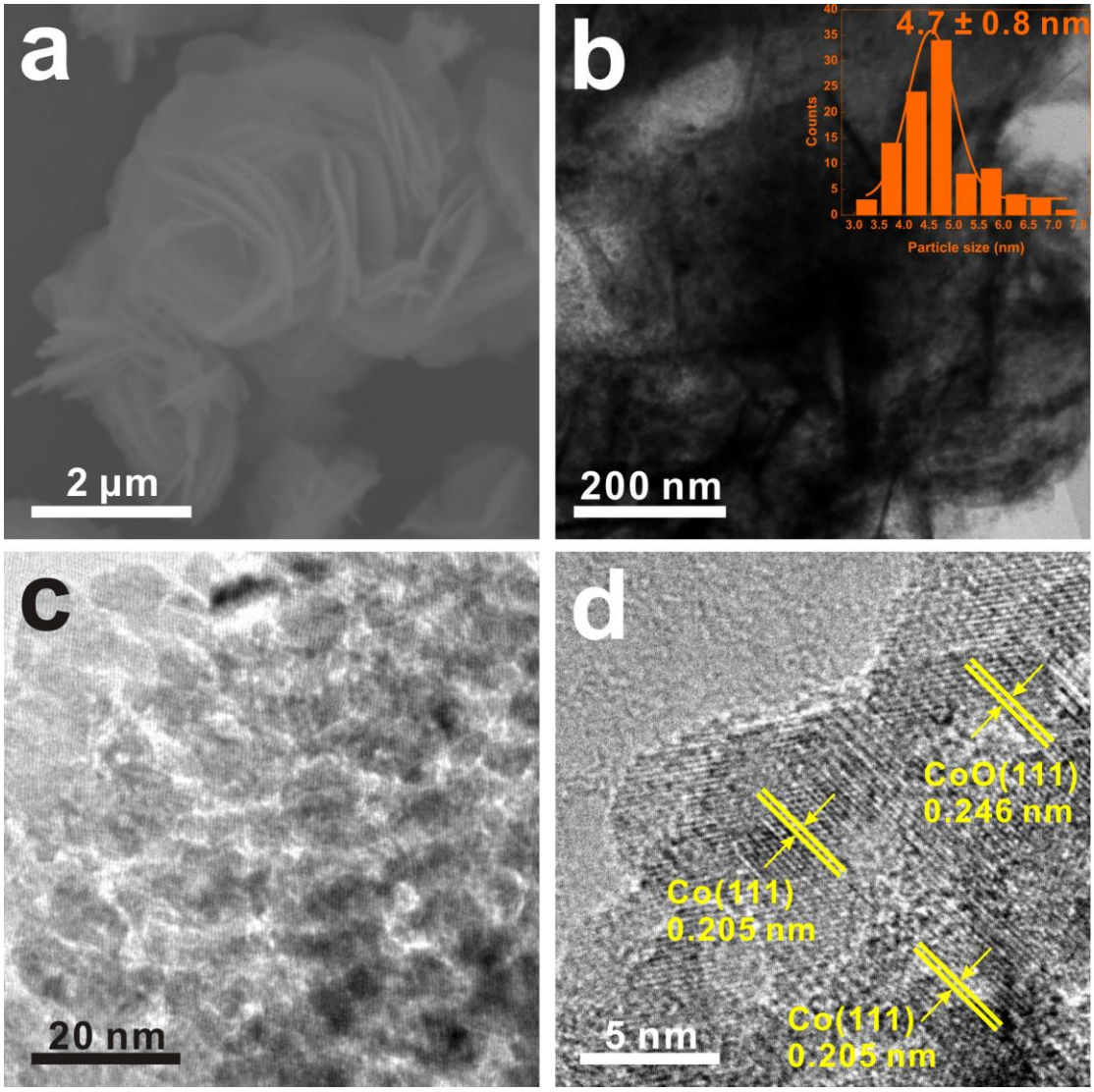

Figure S20. (a) SEM and (b, c) TEM images of $CoAlO_x$ (inset in b: size distribution of the Co and CoO nanoparticles). (d) HRTEM image of metal nanoparticles on $CoAlO_x$, CoO (111) and Co (111) nanofacets are exposed.

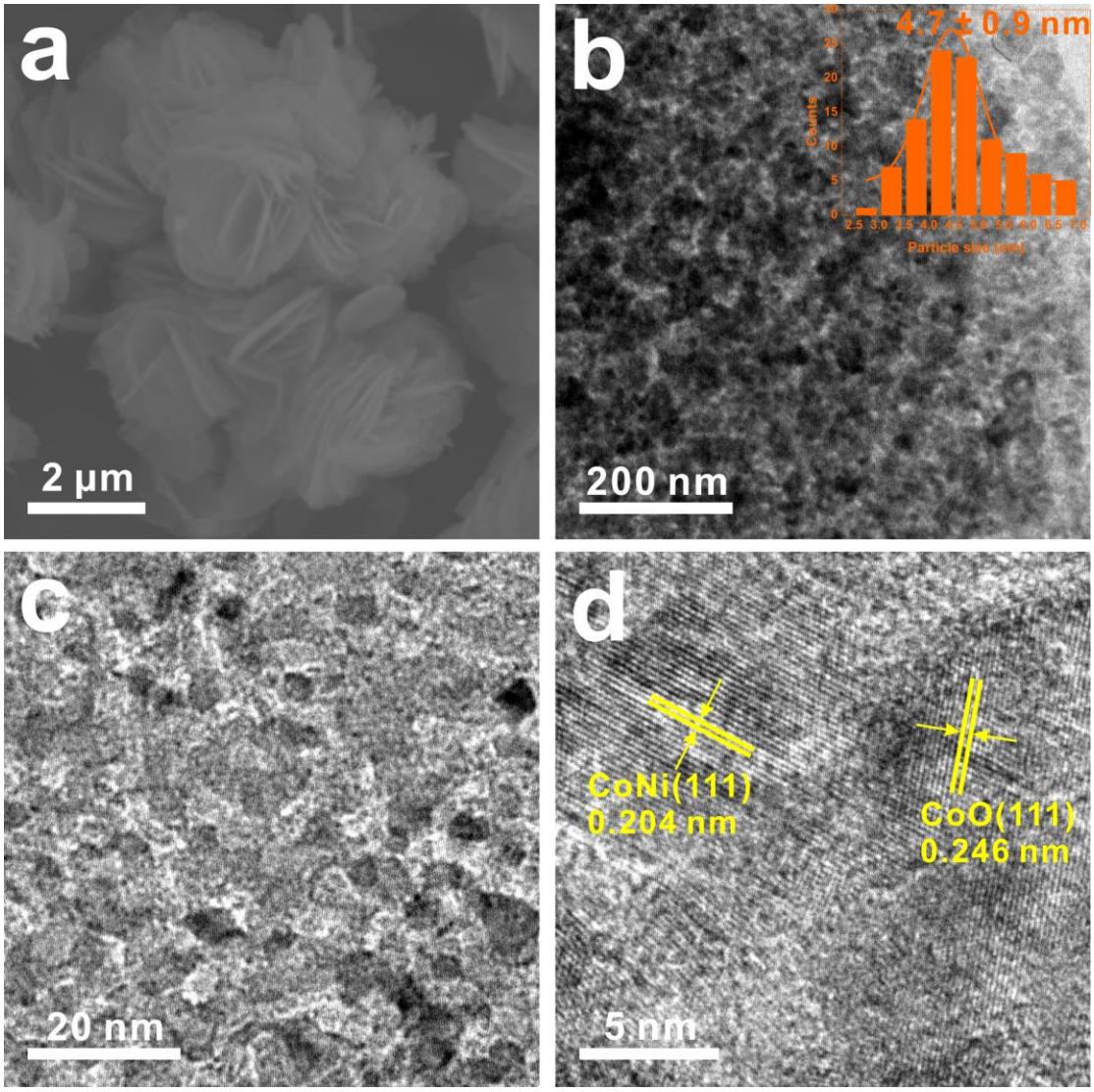

Figure S21. (a) SEM and (b, c) TEM images of $Co_{0.67}Ni_{0.33}AlO_x$ (inset in b: size distribution of the CoNi and CoO nanoparticles). (d) HRTEM image of metal nanoparticles on $Co_{0.67}Ni_{0.33}AlO_x$, CoO (111) and CoNi (111) nanofacets are exposed.

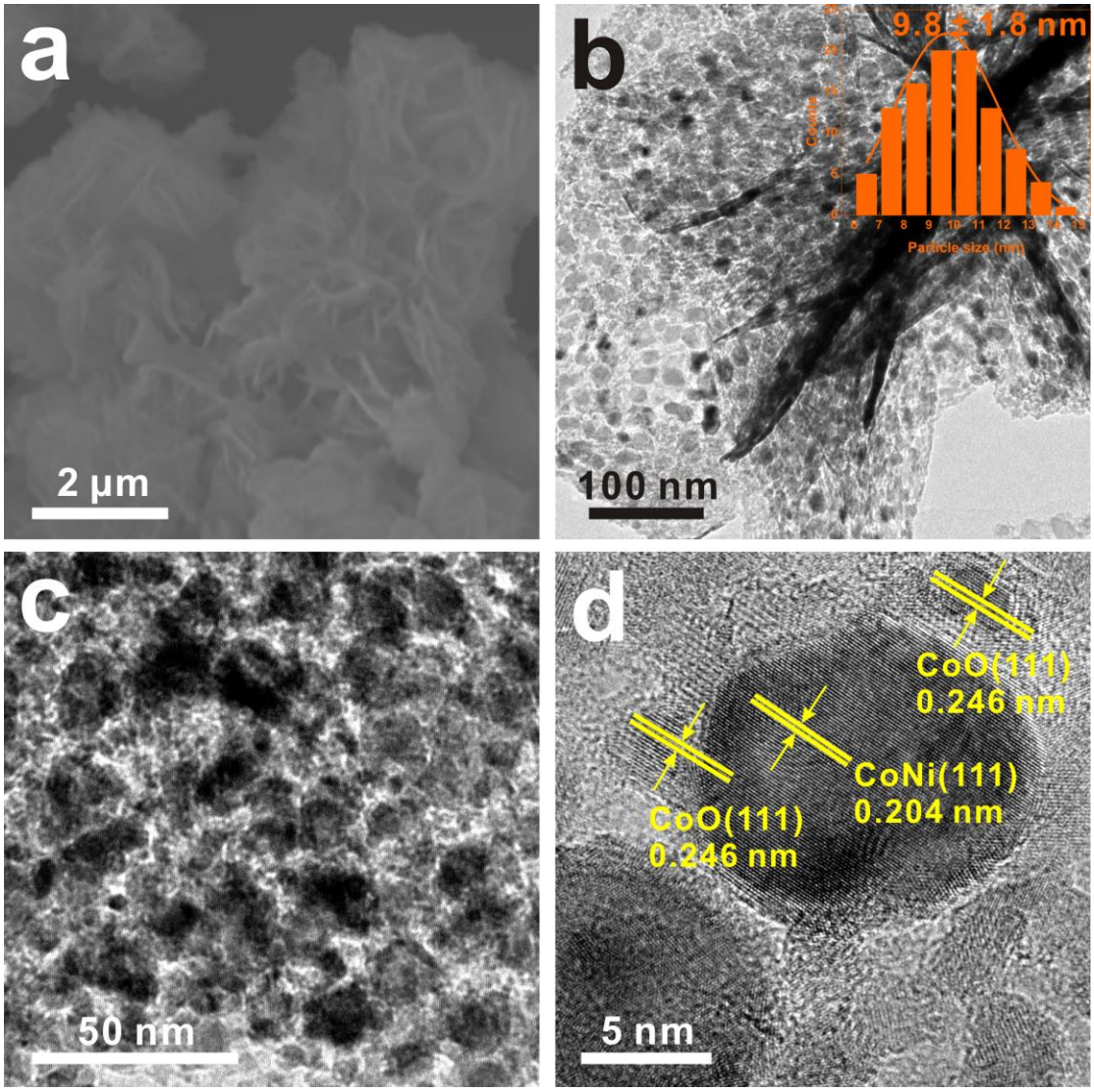

Figure S22. (a) SEM and (b, c) TEM images of $Co_{0.20}Ni_{0.80}AlO_x$ (inset in b: size distribution of the CoNi and CoO nanoparticles). (d) HRTEM image of metal nanoparticles on $Co_{0.20}Ni_{0.80}AlO_x$, CoO (111) and CoNi (111) nanofacets are exposed.

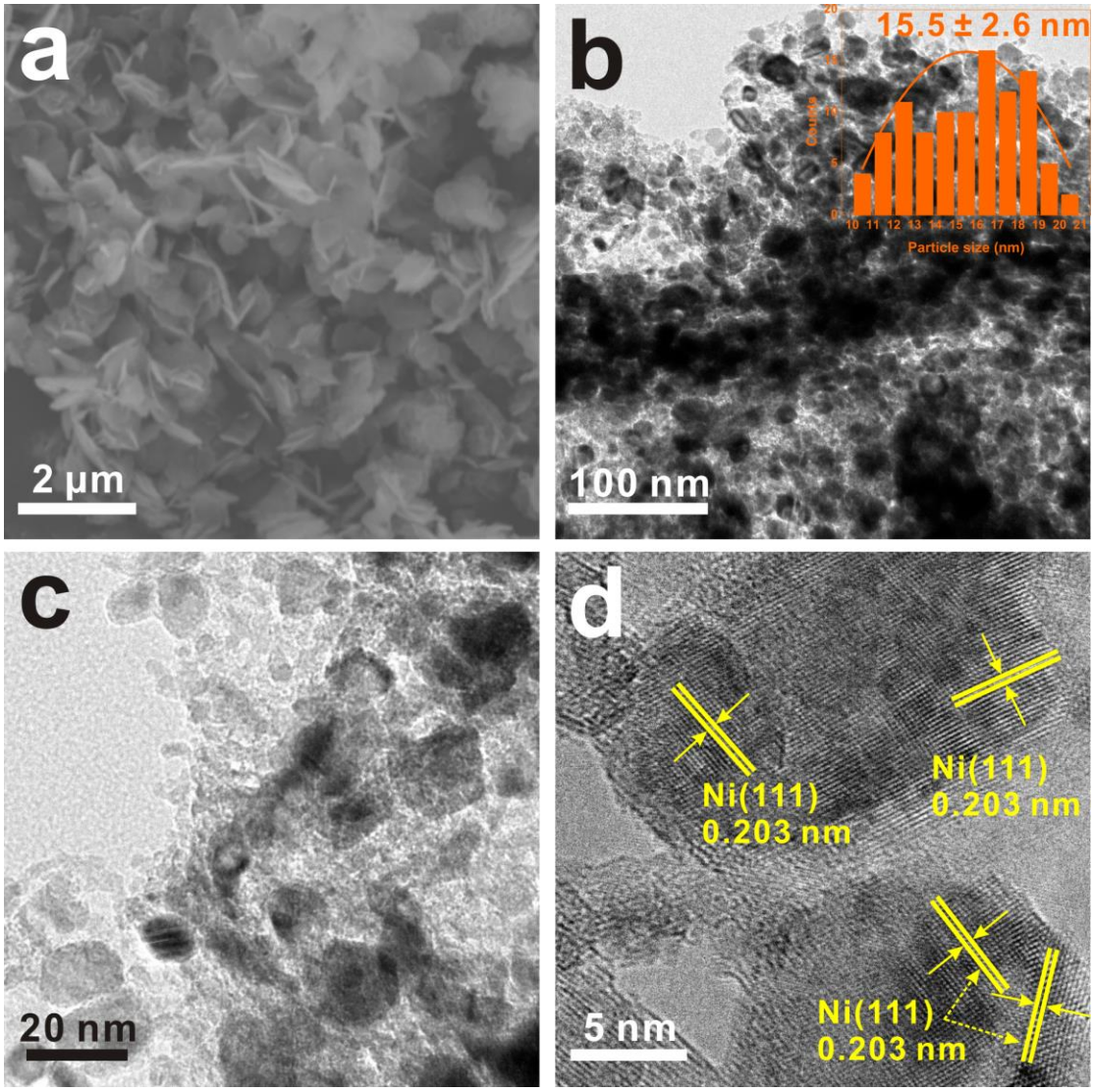

Figure S23. (a) SEM and (b, c) TEM images of $NiAlO_x$ (inset b: size distribution of the Ni nanoparticles). (d) HRTEM image of metal nanoparticles on $NiAlO_x$, Ni (111) nanofacets are exposed.

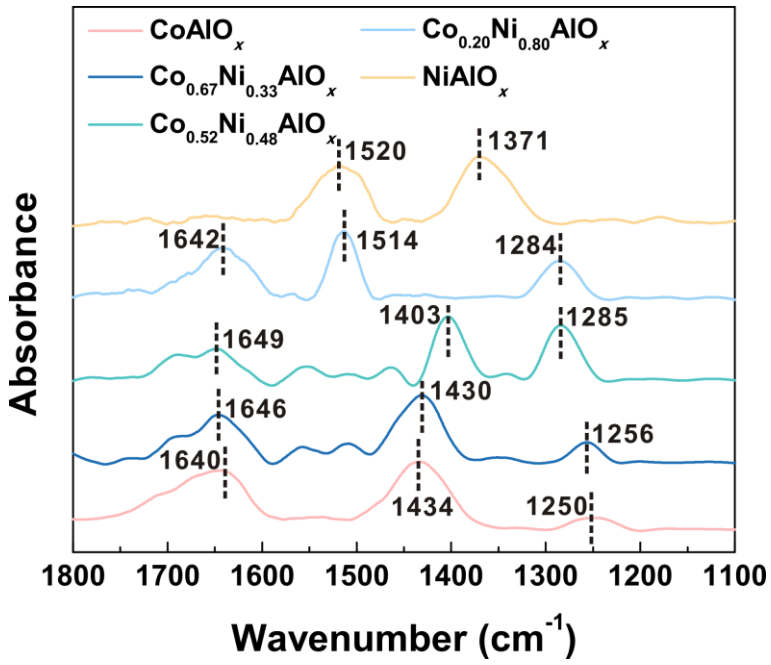

Figure S24. *In-situ* CO_2 adsorption FT-IR spectra of various catalysts at 250 °C.

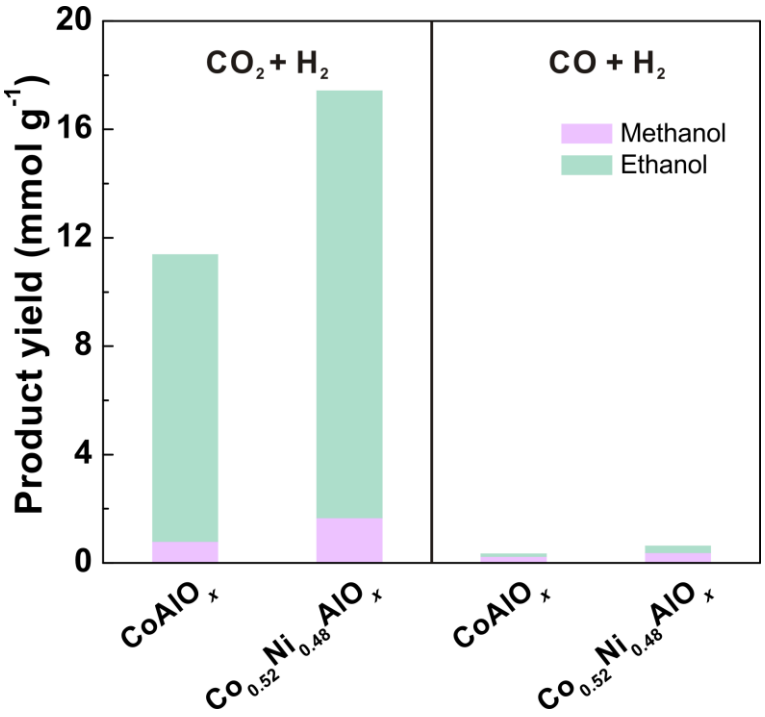

Figure S25. Catalytic performances of $CoAlO_x$ and $Co_{0.52}Ni_{0.48}AlO_x$ catalysts in CO_2 hydrogenation and CO hydrogenation.

Note: The reverse water–gas shift (RWGS) + CO-hydrogenation pathway has been reported for $*CH_x$ formation in the CO_2 hydrogenation, where the initial step is *CO formation *via* the RWGS reaction, and then the *CO species were hydrogenated to *HCO, $*HCOH$, $*H_2COH$, and $*H_3CO$, the C–O bond dissociation leads to $*CH_x$ formation.[1,2] However, this pathway might be excluded on the $CoAlO_x$ and $Co_{0.52}Ni_{0.48}AlO_x$ catalysts because of the poor activity when CO/H_2 was used as feed gas.

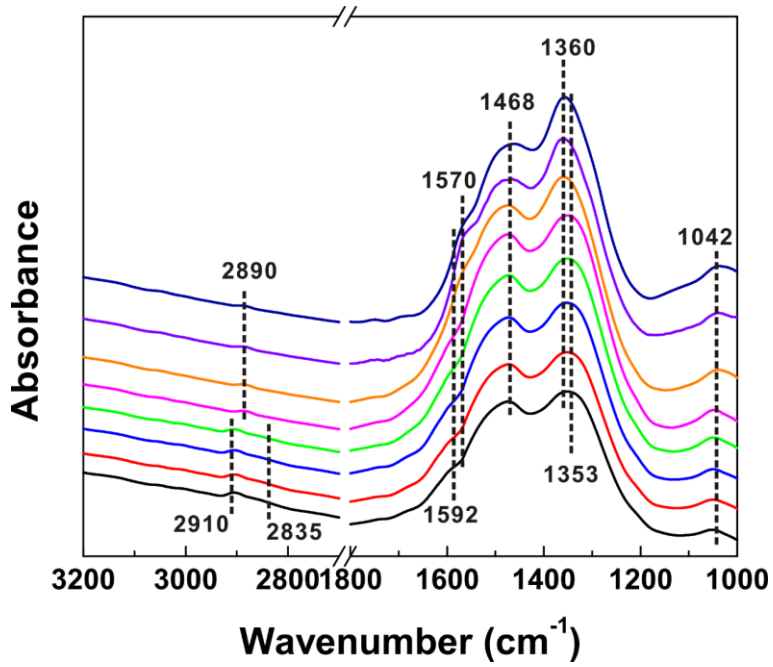

Figure S26. *In-situ* FT-IR spectra of the $Co_{0.67}Ni_{0.33}AlO_x$ catalyst with pre-adsorbed CO_2 and pulsed H_2 at 250 °C (data collected for each 2 min).

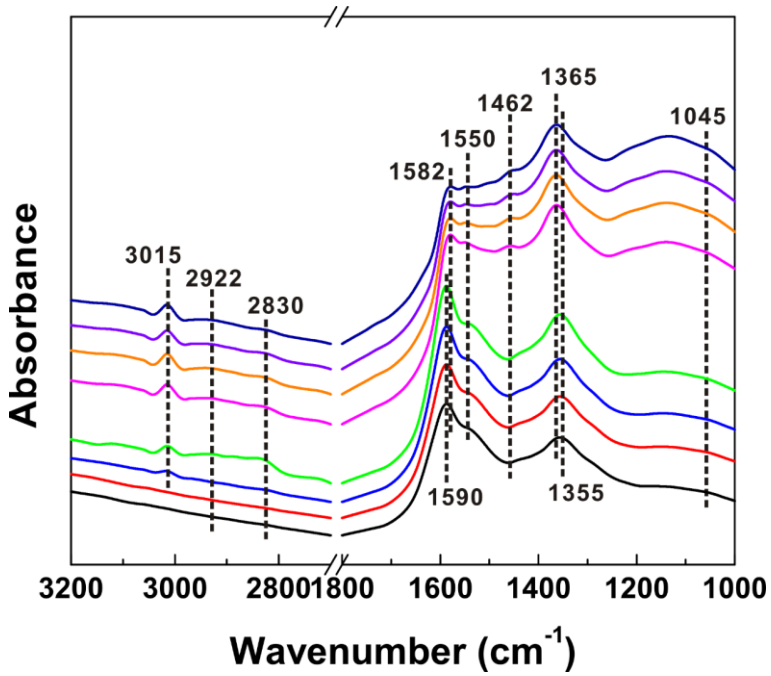

Figure S27. *In-situ* FT-IR spectra of the $Co_{0.20}Ni_{0.80}AlO_x$ catalyst with pre-adsorbed CO_2 and pulsed H_2 at 250 °C (data collected for each 2 min).

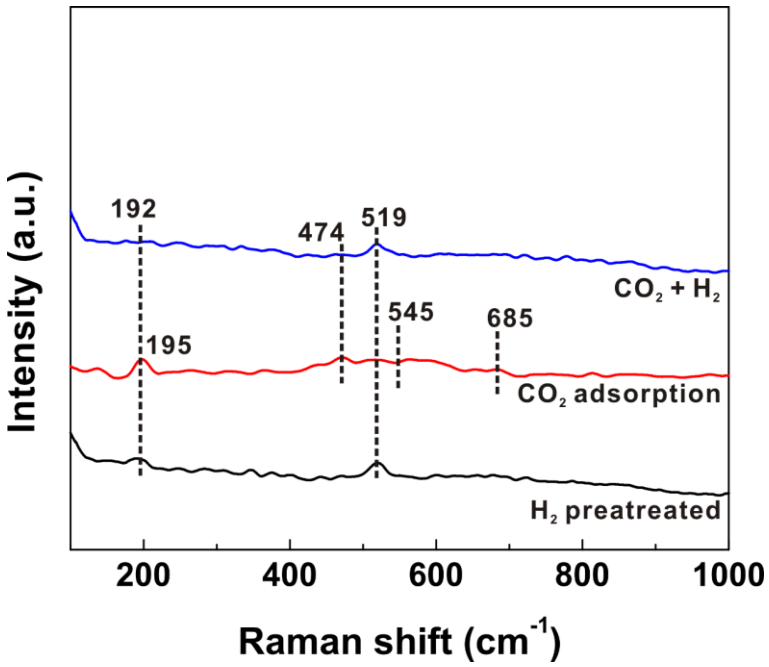

Figure S28. *In-situ* Raman spectra of $Co_{0.52}Ni_{0.48}AlO_x$ catalyst under CO_2 and CO_2+H_2 treatment at 250 °C.

Note: *In-situ* Raman spectra of $Co_{0.52}Ni_{0.48}AlO_x$ catalyst were collected to investigate the change of metal species in CO_2 adsorption and hydrogenation process. In the spectrum of H_2 pretreated $Co_{0.52}Ni_{0.48}AlO_x$ sample, Raman peaks at 192 and 519 cm^{-1} are observed, assigned to Co–O modes.[3,4] Introducing CO_2 gas to the sample leads to the new peaks at 474, 545 and 685 cm^{-1}, accompanied by the blue shift of signal at 192 cm^{-1} to 195 cm^{-1}. That can be attributed to the new Co–O and Ni–O bonds generating for the interaction with CO_2.[5] Furthermore, the CO_2 adsorbed catalyst was regenerated by introducing hydrogen, suggesting the adsorbed CO_2 species on the surface have been eliminated.

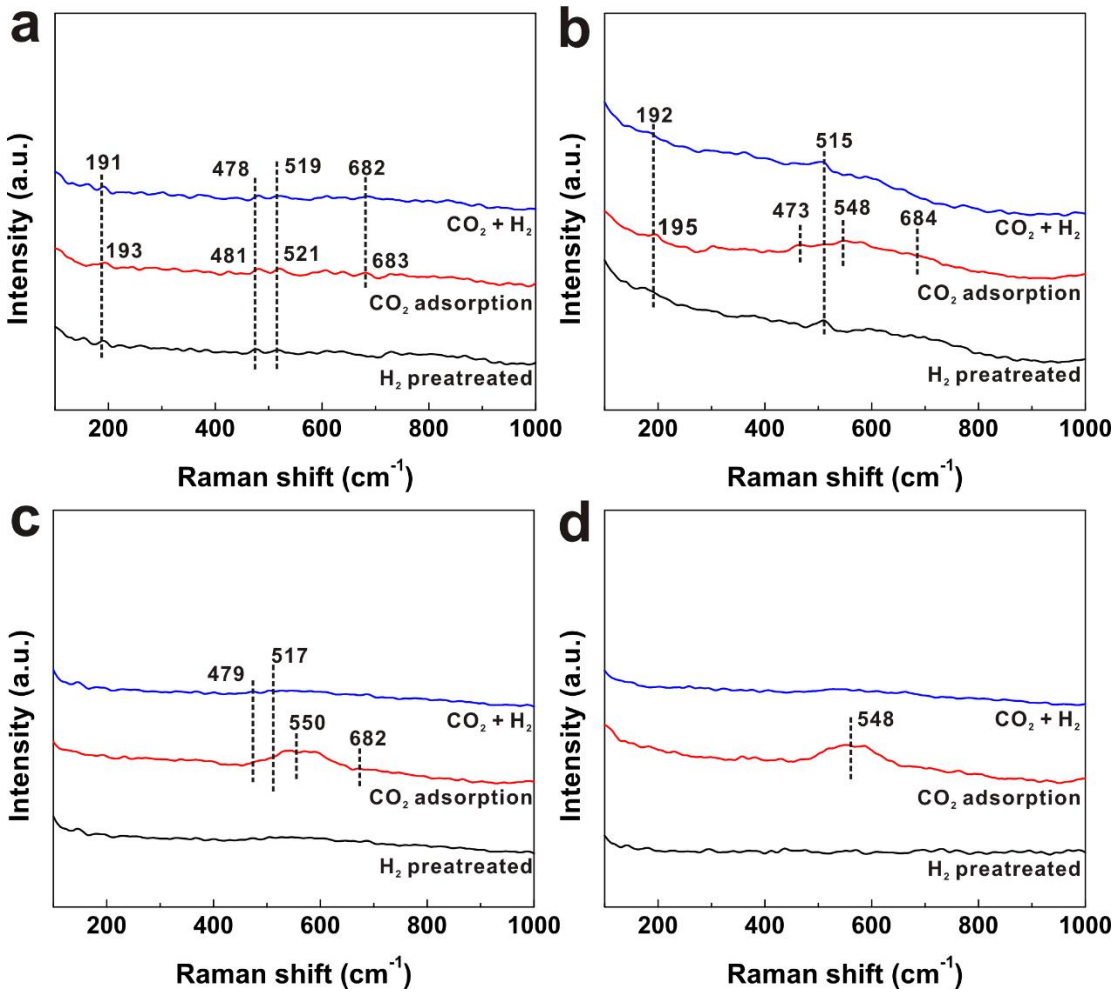

Figure S29. *In-situ* Raman spectra of (a) $CoAlO_x$, (b) $Co_{0.67}Ni_{0.33}AlO_x$, (c) $Co_{0.20}Ni_{0.80}AlO_x$ and (d) $NiAlO_x$ catalysts under CO_2 and CO_2+H_2 treatment at 250 °C.

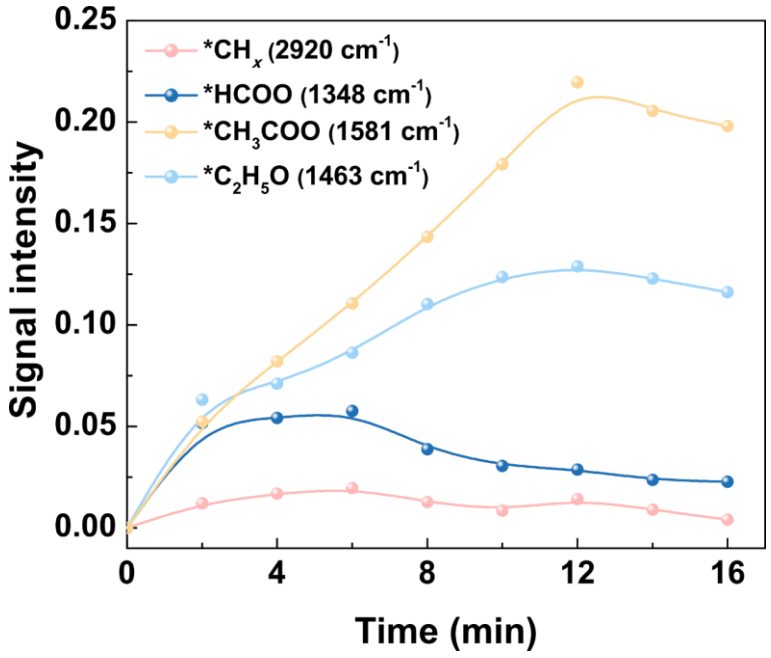

Figure S30. Time dependent FT-IR peak intensity of different reaction intermediates on $Co_{0.52}Ni_{0.48}AlO_x$ catalyst with pulsed H_2 at 250 °C (collected for each 2 min).

Note: Although the exact pathways of ethanol formation are strongly related to the catalyst features, reaction conditions, and feed gases, the coupling between dissociated CO/CO_2 (e.g. $*CH_x$) and undissociated CO/CO_2 (e.g. $*CH_xO$, *CO, *HCOO) are usually regarded as a crucial role.[6] For example, in the RhMn catalyzed syngas-to-ethanol transformation, the CO is dissociated on the Rh sites to form $*CH_x$, which readily inserts into the undissociated CO molecule or primary hydrogenated *CO (HCO* species) adsorbed on the Rh–O–Mn interface as a bridge model to form the C_2-oxygenates. Another pathway was also proposed on such catalyst, CO is dissociated on the Rh–O–Mn interface to form the $*CH_x$, which inserts into another *CO adsorbed on the Rh sites nearby.[7] Similar reaction pathways were also proposed on the other RhMn and RhCu-based catalysts.[8–11]

Computational investigations on ethanol formation over Rh(111) present the reaction routes including hydrogenation of CO to *CHO and $*CH_3O$, C–O cleavage to $*CH_x$, *CO insertion to form $*CH_3CO$, and subsequent hydrogenation to ethanol.[12–14] But methane is always abundantly formed in this case, because of the easily deep hydrogenation of the $*CH_x$ intermediate on the bare Rh surface. Introducing Fe species to Rh surface could hinder the methane formation by stabilizing the $*CH_3$ intermediate and increasing the energy barrier for deep hydrogenation.[13]

Co catalysts have been extensively used for Fischer–Tropsch synthesis. The metallic Co facilitates the CO dissociation and C–C coupling ($*CH_x$ and $*CH_y$ coupling) for carbon chain growth, while Co_2C decreases the activity for CO dissociation, realizing the simultaneously dissociated CO and undissociated CO on the catalyst surface. In addition, the Co_2C exhibits a lower energy barrier for *CO insertion into $*CH_x$ species,[15] leading to the selective formation of C_{2+} oxygenates. In addition to the *CO and $*CH_x$ coupling, the coupling between *CHO and $*CH_x$ was also proposed on the Co surface by DFT calculations.[12] When the Cu promoter was

incorporated into the Co catalyst, a part of the active sites for C–O cleavage and *CH_x coupling were blocked, leading to the low energy barrier for *CO or *CHO insertion.[16]

With regard to the CO_2 hydrogenation to C_{2+} oxygenates, the noble metal-containing catalysts, such as Pt/Co_3O_4, Pd–Cu, and Rh–Fe catalysts,[17–19] catalyzed the hydrogenation of CO_2 into *CO/*HCO intermediates, which readily reacts with the *CH_x species to form the higher carbon products. These catalysts proceed similar reaction pathways in the syngas conversion.

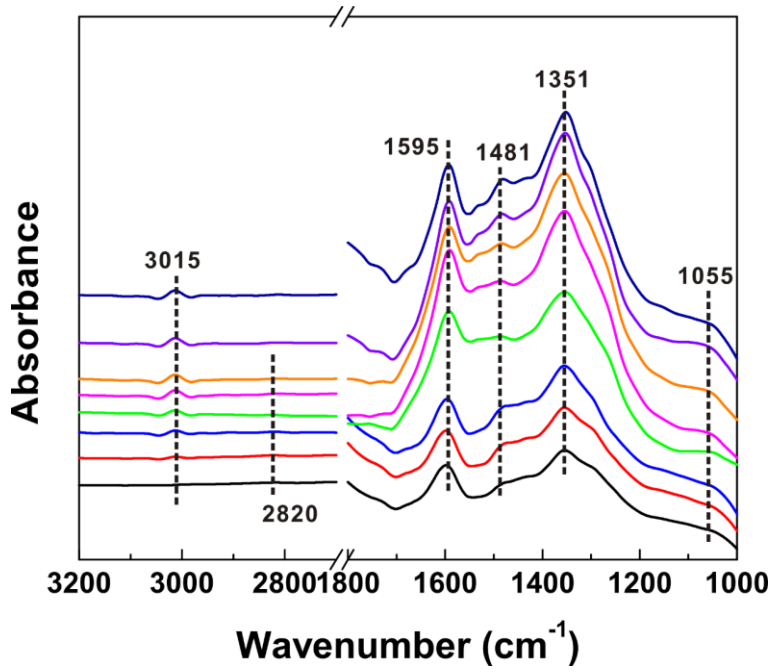

Figure S31. *In-situ* FT-IR spectra of $NiAlO_x$ catalyst under CO_2 and CO_2+H_2 treatment at 250 °C.

Note: $NiAlO_x$ catalyst gives strong IR bands at 1055, 1351, 1595 and 3015 cm^{-1} with H_2 pulsed, indicating that the intermediate of *HCOO species is dominant in the CO_2 hydrogenation, which could be transformed into $*CH_3O$ (1055 and 1481 cm^{-1}).[20–22] In the meanwhile, a large amount of CH_4 is observed, while the $*CH_x$ species are undetectable on $NiAlO_x$ catalyst. It is demonstrated that the Ni-catalyzed methanation of CO_2 is highly efficient, while the formation of $*CH_x$ species is difficult on the $NiAlO_x$.

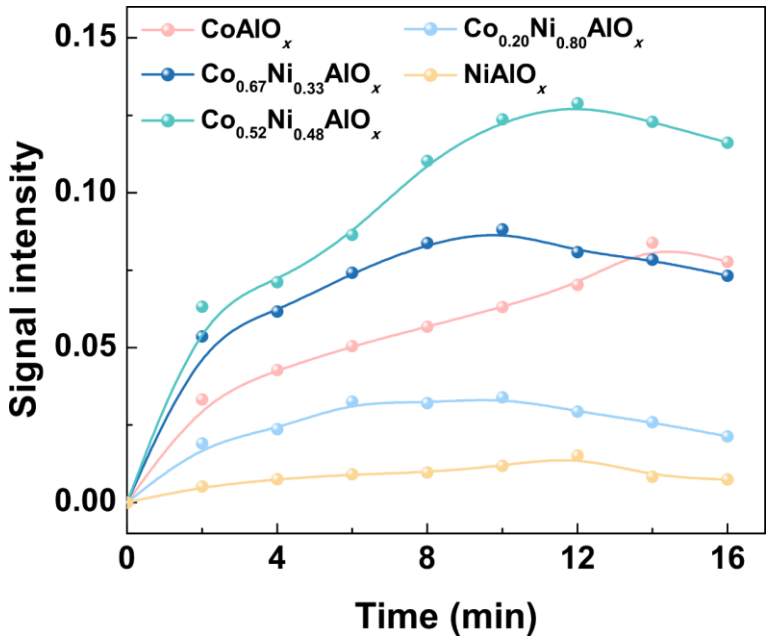

Figure S32. Time dependent FT-IR peak intensity of *C_2H_5O (1463 cm^{-1}) intermediate on various catalyst with pulsed H_2 at 250 °C (collected for each 2 min). The signal of *CH_3O (1481 cm^{-1}) instead of *C_2H_5O on $NiAlO_x$ catalyst is exhibited.

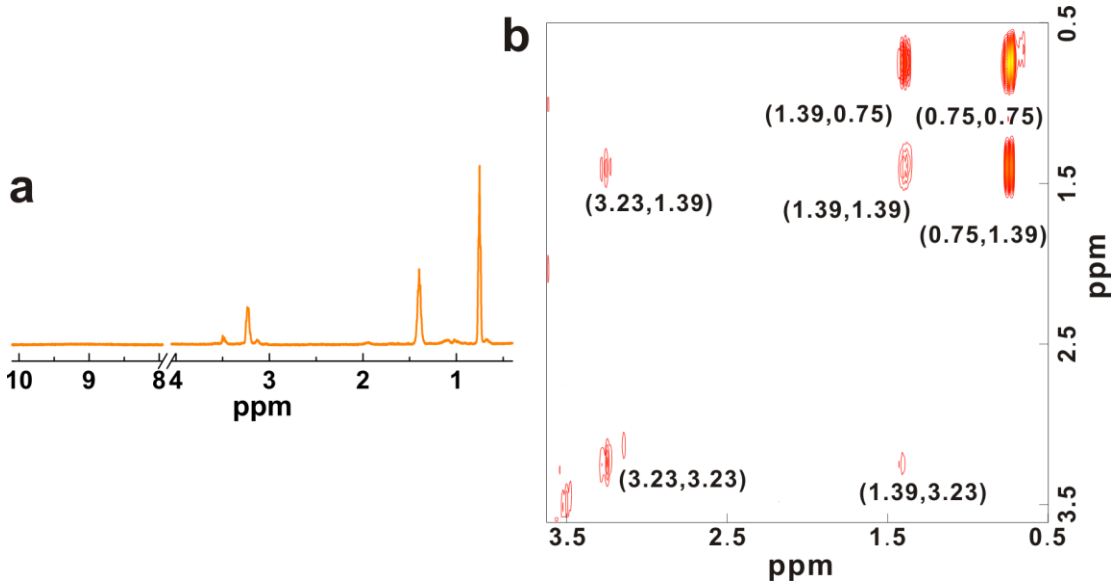

Figure S33. (a) ^{1}H NMR spectrum and (b) ^{1}H COSY NMR spectrum of the mixture in the reactor over $CoAlO_x$ catalyst during the reaction.

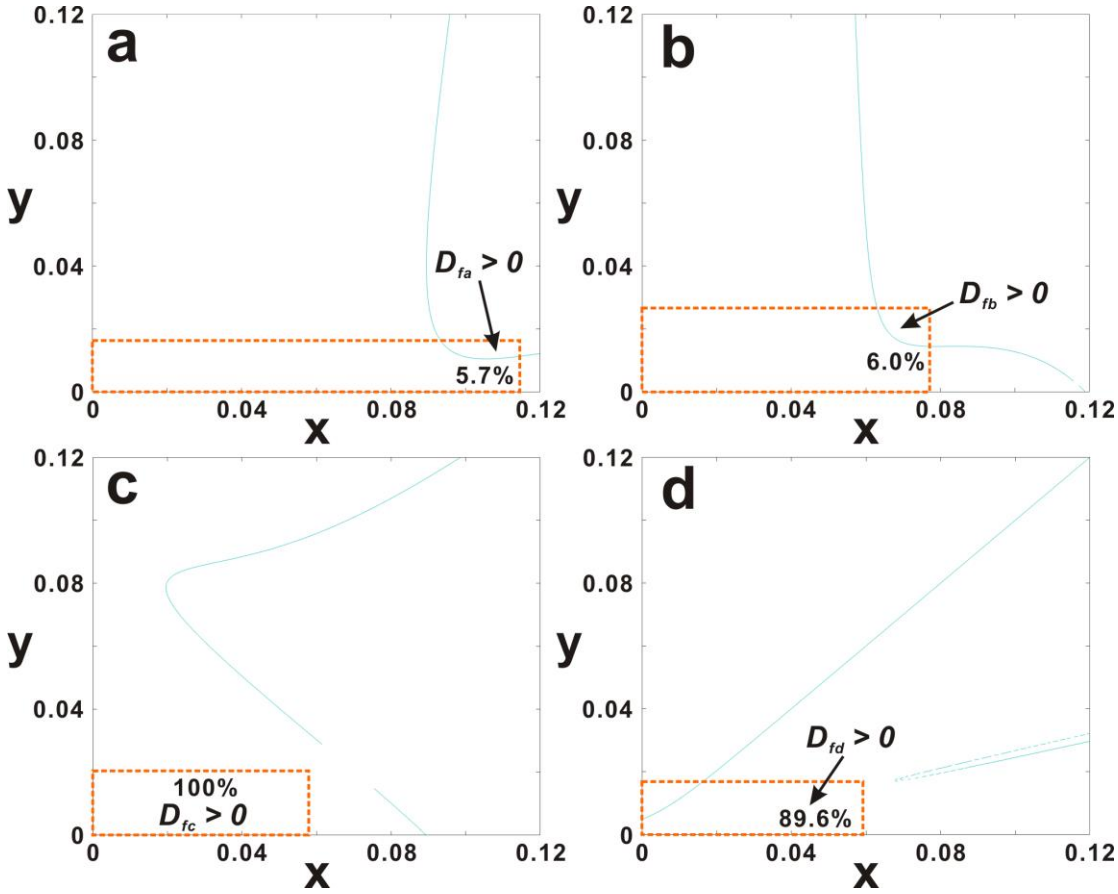

Figure S34. Diagram of D_f>0 for (a) $CoAlO_x$, (b) $Co_{0.67}Ni_{0.33}AlO_x$, (c) $Co_{0.52}Ni_{0.48}AlO_x$, and (d) $Co_{0.20}Ni_{0.80}AlO_x$ catalysts within the experimental parameters. The numbers represent the percentage of overlapped area of D_f>0 to the area of orange rectangles.

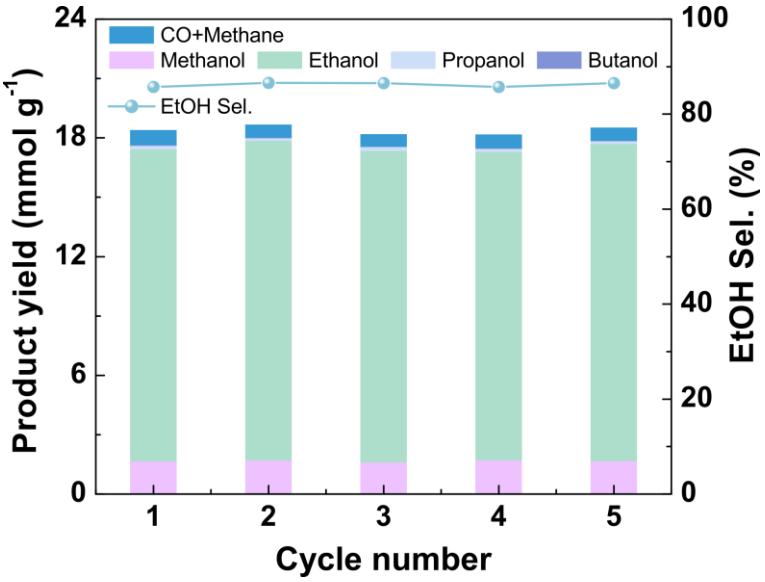

Figure S35. Data characterizing the recyclability of $Co_{0.52}Ni_{0.48}AlO_x$ catalyst in CO_2 hydrogenation. Reaction conditions: catalyst (25 mg), H_2O (2 mL), initial pressure 4.0 MPa (H_2/CO_2 = 3:1), 12 h. The yield and selectivity are based on the number of moles of carbon.

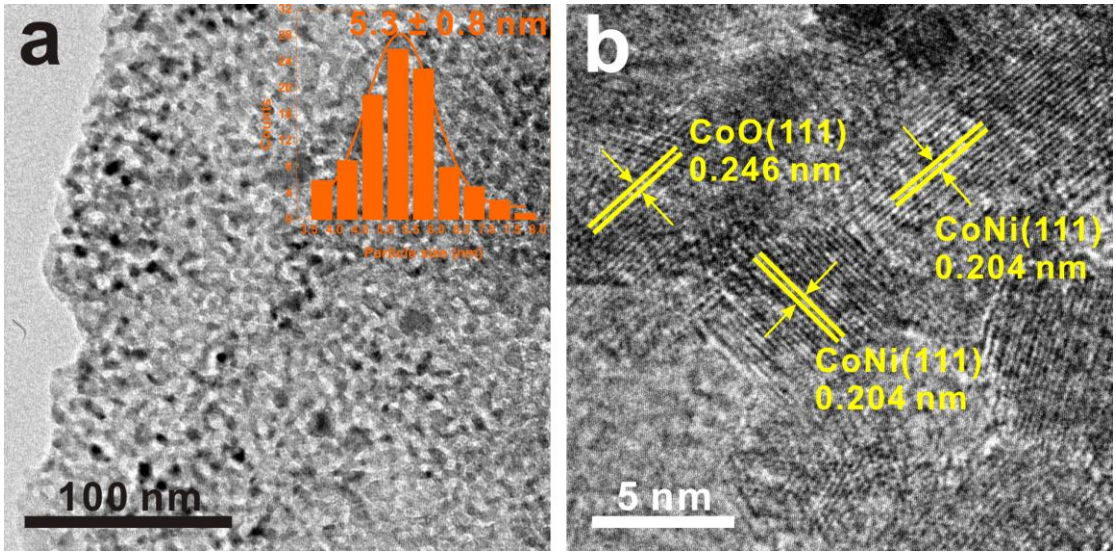

Figure S36. (a) TEM image of $Co_{0.52}Ni_{0.48}AlO_x$ with size distribution of CoNi and CoO nanoparticles, and (b) HRTEM image of $Co_{0.52}Ni_{0.48}AlO_x$ obtained after CO_2 hydrogenation for 5 cycles.

Table S1. Atomic ratio of Co/(Co+Ni) on several catalysts.

Entry	Sample	Co/(Co+Ni) (molar ratio) by ICP analysis
1	$CoAlO_x$	1.00
2	$Co_{0.67}Ni_{0.33}AlO_x$	0.67
3	$Co_{0.52}Ni_{0.48}AlO_x$	0.52
4	$Co_{0.20}Ni_{0.80}AlO_x$	0.20
5	$NiAlO_x$	0
6	$Co_{0.52}Ni_{0.48}AlO_x$[a]	0.53

[a]The sample was obtained after CO_2 hydrogenation for 5 cycles.

Table S2. Comparison of the activities of various catalysts for the CO_2 hydrogenation to ethanol.

Catalyst	Temp. (°C)	Press. (MPa)	H_2/CO_2 ratio	Ethanol sel. (%)	Ethanol yield ($mmol/g_{cat}·h$)	Ref.
$Co_{0.52}Ni_{0.48}AlO_x$-600	200	4	3:1	85.8	1.314	This work
Pt/Co_3O_4	200	8	3:1	57.0	0.29	[17]
$CoAlO_x$-600	200	4	3:1	88.5	0.892	[23]
Pt/Co_3O_4-p	200	2	3:1	4.1	0.56	[24]
$2\%Rh–2.5\%Fe/TiO_2$	270	2	1:1	6.41	1.05	[25]
$0.1Pd/Fe_3O_4$	400	0.1	4:1	17.8	0.846	[26]
CoMoS	310	10.3	1:1	4.2	0.6	[27]
$Mo_1Co_1K_{0.6}$	320	5	3:1	12.9	0.143	[28]
Au/TiO_2	200	6	3:1	>99	2.82	[29]
$Au/a\text{-}TiO_2$	200	6	3:1	>99	2.90	[30]

Note: The $Co_{0.52}Ni_{0.48}AlO_x$-600 catalyst exhibited ethanol productivity at 1.314 $mmol/g_{cat}·h$, which is significantly higher than the cobalt and Pt–Co catalysts. The other Rh and Pd containing catalysts exhibited the ethanol productivity at 0.846–1.05 $mmol/g_{cat}·h$. These data further confirm the high efficiency of $Co_{0.52}Ni_{0.48}AlO_x$-600 catalyst in the ethanol production. The Au catalysts are reported to be highly efficient, giving the ethanol productivity at 2.82–2.90 $mmol/g_{cat}·h$. Although these productivities are higher than $Co_{0.52}Ni_{0.48}AlO_x$-600 catalyst, the noble-metal free feature of $Co_{0.52}Ni_{0.48}AlO_x$-600 is advantageous for the catalyst cost compared with the Au-based catalyst.

Table S3. *In-situ* FT-IR data of CO_2 hydrogenation over various catalysts.

Catalysts	Species	Time (min)							
		2	4	6	8	10	12	14	16
$CoAlO_x$	*HCOO	0.0741	0.0815	0.1055	0.1146	0.0851	0.0741	0.0676	0.0633
	*CH_x	0.0091	0.0123	0.0166	0.0058	0.0032	0	0	0
	C_2	0.0715	0.1104	0.1401	0.1597	0.1767	0.1719	0.1717	0.1511
$Co_{0.67}Ni_{0.33}AlO_x$	*HCOO	0.0466	0.0528	0.0614	0.0687	0.0768	0.0585	0.0548	0.0522
	*CH_x	0.0112	0.0211	0.0258	0.0106	0.0073	0.0039	0	0
	C_2	0.089	0.1167	0.1561	0.2019	0.22	0.1899	0.167	0.1533
$Co_{0.52}Ni_{0.48}AlO_x$	*HCOO	0.0517	0.0542	0.0576	0.0388	0.0305	0.0288	0.0237	0.0228
	*CH_x	0.0121	0.017	0.0197	0.0127	0.0086	0.0142	0.009	0.0041
	C_2	0.1156	0.1532	0.197	0.2537	0.3029	0.3485	0.3285	0.3143
$Co_{0.20}Ni_{0.80}AlO_x$	*HCOO	0.0345	0.0397	0.0479	0.0593	0.0449	0.0378	0.0374	0.0348
	*CH_x	0.0086	0.0101	0.0124	0.0111	0.0109	0.0164	0.0083	0.0046
	C_2	0.0428	0.0536	0.0772	0.0886	0.0971	0.0778	0.0635	0.0498

Table S4. Parameters and fitting degrees for model *z(x, y)*.

Samples	$CoAlO_x$	$Co_{0.67}Ni_{0.33}AlO_x$	$Co_{0.52}Ni_{0.48}AlO_x$	$Co_{0.20}Ni_{0.80}AlO_x$
p_1	2.2023	59.3444	-16.7294	-459.5026
p_2	-1259.7240	-2458.9751	7.5414	1763.2566
p_3	11.0702	47.9396	2.7081	43.4390
p_4	-59.9160	-412.9750	-28.2441	-13435.2386
p_5	7.5387	-10.2075	-35.6725	50723.2481
p_6	2385.2130	1760.6952	-256.6471	76.6529
R^2	0.98807	0.99740	0.99624	0.98540
Adj. R^2	0.97217	0.99392	0.99122	0.96593
RMSE	0.003726	0.002077	0.004994	0.002195
SSR	0.000111	0.000035	0.000200	0.000039

RMSE: root-mean-square error. SSR: sum of squares of the regression. Adj. R^2: adjusted R-square.

Table S5. Model *z(x, y)* for various catalysts.

z(x, y)	$z=\frac{1+p_1x+p_2y}{p_3(1+k_1x+k_2y)}+p_6xy$	(1.4)
$CoAlO_x$	$z=\frac{1+2.2023x-1259.7y}{11.0702(1-5.4124x+0.6810y)}+2385.2xy$	(1.5)
$Co_{0.67}Ni_{0.33}AlO_x$	$z=\frac{1+59.3444x-2459.0y}{47.9396(1-8.6145x-0.2129y)}+1760.7xy$	(1.6)
$Co_{0.52}Ni_{0.48}AlO_x$	$z=\frac{1-16.7290x+7.5414y}{2.7081(1-10.4295x-13.1723y)}-256.6xy$	(1.7)
$Co_{0.20}Ni_{0.80}AlO_x$	$z=\frac{1-459.5026x+1763.3y}{43.4390(1-309.2898x+1167.7y)}+76.7xy$	(1.8)

Table S6. The partial derivative $z\ (\frac{dz}{dx},\ \frac{dz}{dy})$ for various catalysts.

Catalysts	Partial derivative $z\ (\frac{dz}{dx},\ \frac{dz}{dy})$	
$CoAlO_x$	$\frac{dz}{dx} = \frac{84.2959-75461.0y}{[11.0702(1-5.4124x+0.6810y)]^2} + 2385.2y$	(1.10)
	$\frac{dz}{dy} = \frac{-13953.0+75461.0x}{[11.0702(1-5.4124x+0.6810y)]^2} + 2385.2x$	(1.11)
$Co_{0.67}Ni_{0.33}AlO_x$	$\frac{dz}{dx} = \frac{3257.9-1016100.0y}{[47.9396(1-8.6145x-0.2129y)]^2} + 1760.7y$	(1.12)
	$\frac{dz}{dy} = \frac{-117870.0+1016100.0x}{[47.9396(1-8.6145x-0.2129y)]^2} + 1760.7x$	(1.13)
$Co_{0.52}Ni_{0.48}AlO_x$	$\frac{dz}{dx} = \frac{-17.0598+809.7562y}{[2.7081(1-10.4295x-13.1723y)]^2} - 256.6y$	(1.14)
	$\frac{dz}{dy} = \frac{56.0949-809.7562x}{[2.7081(1-10.4295x-13.1723y)]^2} - 256.6x$	(1.15)
$Co_{0.20}Ni_{0.80}AlO_x$	$\frac{dz}{dx} = \frac{-6525.0+382490.0y}{[43.4390(1-309.2898x+1167.7y)]^2} + 76.7y$	(1.16)
	$\frac{dz}{dy} = \frac{25871.0-382490.0x}{[43.4390(1-309.2898x+1167.7y)]^2} + 76.7x$	(1.17)

Table S7. The difference $D_f = \frac{dz}{dy} - \frac{dz}{dx}$ for various catalysts.

Catalysts	$D_f = \frac{dz}{dy} - \frac{dz}{dx}$	
$CoAlO_x$	$D_{fa} = \frac{-615.7584\ (0.1860-(x+y))}{(1-5.4124x+0.6810y)^2} + 2385.2(x-y)$	(1.18)
$Co_{0.67}Ni_{0.33}AlO_x$	$D_{fb} = \frac{-442.1271(0.1192-(x+y))}{(1-8.6145x-0.2129y)^2} + 1760.7(x-y)$	(1.19)
$Co_{0.52}Ni_{0.48}AlO_x$	$D_{fc} = \frac{110.4142(0.0903-(x+y))}{(1-10.4295x-13.1723y)^2} - 256.6(x-y)$	(1.20)
$Co_{0.20}Ni_{0.80}AlO_x$	$D_{fd} = \frac{202.7020(0.0847-(x+y))}{(1-309.2898x+1167.7y)^2} + 76.7(x-y)$	(1.21)

Mathematical model study

The relationship between the *HCOO, *CH_x and C_2 (*CH_3COO+*C_2H_5O) species were further investigated by mathematic modelling. 1stOpt software package (First Optimization, Data Processing System) was employed for data processing and analyzing. Considering the catalytic kinetic feature of *CH_x species insertion into *HCOO, we expect to adapt the reaction rate theory in physical chemistry which might help to create a reasonable model for this heterogeneous catalytic reaction.

For a reaction as A + B → C + D, the reaction rate (r) follow the Langmuir-Hinshelwood-Hougen-Watson (LHHW) kinetic equation[31,32] applying to only one rate-determining step (adsorption, surface reaction, or desorption) while the other steps are in quasi-equilibria.

$$r = \frac{kinetic\ factor \times driving\ force}{(adsorption\ term)^n} \quad (1.1)$$

For CO_2 hydrogenation to ethanol over Co–Ni catalysts, the C-C coupling (*HCOO + *CH_x → *CH_3COO + *C_2H_5O) is regarded as a key step, which is limited by the generation of C_1 intermediates on the catalyst surface. Given the *in-situ* FT-IR data (Table S3) of CO_2 hydrogenation over $CoAlO_x$, $Co_{0.67}Ni_{0.33}AlO_x$, $Co_{0.52}Ni_{0.48}AlO_x$ and $Co_{0.20}Ni_{0.80}AlO_x$ catalysts, the QuickFit ToolBox module in 1stOpt software provided several alternative functions which might fit these samples on the basis of the optimization algorithm of Universal Global Optimization (UGO). Combining the catalytic kinetic model and the fitting mathematical formulas, we propose a model *z(x, y)* with equation 1.2 to represent the catalytic process integrating all the abovementioned catalysts.[33]

$$z = \frac{1+p_1x+p_2y}{p_3+p_4x+p_5y} + p_6xy \quad (1.2)$$

Where p_1 to p_6 are parameters given by nonlinear regression fitting of experimental data. *x, y* and *z* represent the amounts of *HCOO, *CH_x and *CH_3COO + *C_2H_5O, respectively. The $\frac{1+p_1x+p_2y}{p_3+p_4x+p_5y}$ is regarded as the dominant term, while p_6xy is a correction term.

As shown in Table S4, four model *z(x, y)* for several samples are well fitted, with R^2 close to 1 (> 0.985) and *RMSE* close to 0 (< 0.01).

For the convenience of subsequent analysis, the model *z(x, y)* (Table S5) is trimmed to:

$$z = \frac{1+p_1x+p_2y}{p_3(1+k_1x+k_2y)} + p_6xy \quad (1.3)$$

Where k_1 and k_2 are defined as $k_1 = \frac{p_4}{p_3}$ and $k_2 = \frac{p_5}{p_3}$, respectively.

In order to find whether *HCOO or *CH_x species have more impact on the generation of C_2 species. The partial derivative $z\ (\frac{dz}{dx}, \frac{dz}{dy})$ and the difference $D_f = \frac{dz}{dy} - \frac{dz}{dx}$ (1.9) were calculated (Tables S6 and S7). The $\frac{dz}{dx}$ and $\frac{dz}{dy}$ represent the impact of the amount of *HCOO and *CH_x species on the amount of *CH_3COO + *C_2H_5O species, respectively. Therefore, the different $D_f = \frac{dz}{dy} - \frac{dz}{dx}$ compares the influences of *CH_x and *HCOO species to *CH_3COO+*C_2H_5O production in the catalytic process.

Moreover, it is concluded that the D_f on various catalysts, which provide the equation for forecasting the reaction trend of C_2 species formation derived from the C_1 intermediate amounts. As shown in Figure S34, the $D_f > 0$ is satisfied for all the samples, which means *CH_x exhibits a more positive impact on the C_2 species generation than that of *HCOO. The $CoAlO_x$, $Co_{0.67}Ni_{0.33}AlO_x$, $Co_{0.52}Ni_{0.48}AlO_x$ and $Co_{0.20}Ni_{0.80}AlO_x$ samples exhibit ratios of 5.7, 6.0, 100, and 89.6% for $CoAlO_x$, $Co_{0.67}Ni_{0.33}AlO_x$, $Co_{0.52}Ni_{0.48}AlO_x$ and $Co_{0.20}Ni_{0.80}AlO_x$ catalysts within the experimental parameters of *x* and *y*, respectively. These data confirm the best C_2 formation trend on $Co_{0.52}Ni_{0.48}AlO_x$.

References

(1) Kattel, S.; Yu, W.; Yang, X.; Yan, B.; Huang, Y.; Wan, W.; Liu, P.; Chen, J. G. CO_2 Hydrogenation over Oxide-Supported PtCo Catalysts: The Role of the Oxide Support in Determining the Product Selectivity. *Angew. Chem. Int. Ed.* **2016**, *55*, 7968–7973.

(2) Kattel, S.; Yan, B.; Chen, J. G.; Liu, P. CO_2 Hydrogenation on Pt, Pt/SiO_2 and Pt/TiO_2: Importance of Synergy between Pt and Oxide Support *J. Catal.* **2016**, *343*, 115−126.

(3) Jiang, J.; Li, L. Synthesis of Sphere-Like Co_3O_4 Nanocrystals via a Simple Polyol Route. *Mater. Lett.* **2007**, *61*, 4894–4896.

(4) Yang, J.; Liu, H.; Martens, W. N.; Frost, T. L. Synthesis and Characterization of Cobalt Hydroxide, Cobalt Oxyhydroxide, and Cobalt Oxide Nanodiscs. *J. Phys. Chem. C* **2010**, *114*, 111–119.

(5) Wang, W.; Liu, Y.; Xu, C.; Zheng, C.; Wang, G. Synthesis of NiO Nanorods by a Novel Simple Precursor Thermal Decomposition Approach. *Chem. Phys. Lett.* **2002**, *362*, 119–122.

(6) Luk, H. T.; Mondelli, C.; Ferré, D. C.; Stewart, J. A.; Pérez-Ramírez, J. Status and Prospects in Higher Alcohols Synthesis from Syngas. *Chem. Soc. Rev.* **2017**, *46*, 1358–1426.

(7) Wang, Y.; Luo, H.; Liang, D.; Bao, X. Different Mechanisms for the Formation of Acetaldehyde and Ethanol on the Rh–Based Catalysts. *J. Catal.* **2000**, *196*, 46–55.

(8) Li, F.; Jiang, D.; Zeng, X. C.; Chen, Z. Mn Monolayer Modified Rh for Syngas-to-Ethanol Conversion: A First-Principles Study. *Nanoscale* **2012**, *4*, 1123–1129.

(9) Wang, J.; Liu, Z.; Zhang, R.; Wang, B. Ethanol Synthesis from Syngas on the Stepped Rh(211) Surface: Effect of Surface Structure and Composition. *J. Phys. Chem. C* **2014**, *118*, 22691–22701.

(10) Zhao, Y. H.; Yang, M. M.; Sun, D.; Su, H. Y.; Sun, K.; Ma, X.; Bao, X.; Li, W. X. Rh-Decorated Cu Alloy Catalyst for Improved C_2 Oxygenate Formation from Syngas. *J. Phys. Chem. C* **2011**, *115*, 18247–18256.

(11) Mei, D.; Rousseau, R.; Kathmann, S. M.; Glezakou, V. A.; Engelhard, M. H.; Jiang, W.; Wang, C.; Gerber, M. A.; White, J. F.; Stevens, D. J. Ethanol Synthesis from Syngas over Rh-Based/SiO_2 Catalysts: A Combined Experimental and Theoretical Modeling Study. *J. Catal.* **2010**, *271*, 325–342.

(12) Zhao, Y. H.; Sun, K.; Ma, X.; Liu, J.; Sun, D.; Su, H. Y.; Li, W. X. Carbon Chain Growth by Formyl Insertion on Rhodium and Cobalt Catalysts in Syngas Conversion. *Angew. Chem. Int. Ed.* **2011**, *50*, 5335–5338.

(13) Choi, Y.; Liu, P. Mechanism of Ethanol Synthesis from Syngas on Rh(111). *J. Am. Chem. Soc.* **2009**, *131*, 13054–13061.

(14) Kapur, N.; Hyun, J.; Shan, B.; Nicholas, J. B.; Cho, K. Ab Initio Study of CO Hydrogenation to Oxygenates on Reduced Rh Terraces and Stepped Surfaces. *J. Phys. Chem. C* **2010**, *114*, 10171–10182.

(15) Pei, Y. P.; Liu, J. X.; Zhao, Y. H.; Ding, Y. J.; Liu, T.; Dong, W. D.; Zhu, H. J.; Su, H. Y.; Yan, L.; Li, J. L.; Li, W. X. High Alcohols Synthesis via Fischer–Tropsch Reaction at Cobalt Metal/Carbide Interface. *ACS Catal.* **2015**, *5*, 3620–3624.

(16) Xu, X. C.; Su, J.; Tian, P.; Fu, D.; Dai, W.; Mao, W.; Yuan, W. K.; Xu, J.; Han, Y. F. First-Principles Study of C_2 Oxygenates Synthesis Directly from Syngas over CoCu Bimetallic Catalysts. *J. Phys. Chem. C* **2015**, *119*, 216–227.

(17) He, Z.; Qian, Q.; Ma, J.; Meng, Q.; Zhou, H.; Song, J.; Liu, Z.; Han, B. Water-Enhanced Synthesis of Higher Alcohols from CO_2 Hydrogenation over a Pt/Co_3O_4 Catalyst under Milder Conditions. *Angew. Chem. Int. Ed.* **2016**, *55*, 737–741.
(18) Bai, S.; Shao, Q.; Wang, P.; Dai, Q.; Wang, X.; Huang, X. Highly Active and Selective Hydrogenation of CO_2 to Ethanol by Ordered Pd–Cu Nanoparticles. *J. Am. Chem. Soc.* **2017**, *139*, 6827–6830.
(19) Yang, C.; Mu, R.; Wang, G.; Song, J.; Tian, H.; Zhao, Z. J.; Gong, J. Hydroxyl-Mediated Ethanol Selectivity of CO_2 Hydrogenation. *Chem. Sci.* **2019**, *10*, 3161–3167.
(20) Graciani, J.; Mudiyanselage, K.; Xu, F.; Baber, A. E.; Evans, J.; Senanayake, S. D.; Stacchiola, D. J.; Liu, P.; Hrbek, J.; Sanz, J. F.; Rodriguez, J. A. Highly Active Copper–Ceria and Copper–Ceria–Titania Catalysts for Methanol Synthesis from CO_2. *Science* **2014**, *345*, 546–550.
(21) Kattel, S.; Yan, B.; Yang, Y.; Chen, J. G.; Liu, P. Optimizing Binding Energies of Key Intermediates for CO_2 Hydrogenation to Methanol over Oxide-Supported Copper. *J. Am. Chem. Soc.* **2016**, *138*, 12440–12450.
(22) Fisher, I. A.; Bell, A. T. In-Situ Infrared Study of Methanol Synthesis from H_2/CO_2 over Cu/SiO_2 and $Cu/ZrO_2/SiO_2$. *J. Catal.* **1997**, *172*, 222–237.
(23) Wang, L.; Wang, L.; Zhang, J.; Liu, X.; Zhang, W.; Yang, Q.; Ma, J.; Dong, X.; Yoo, S. J.; Kim, J. G.; Meng, X.; Xiao, F.-S. Selective Hydrogenation of CO_2 to Ethanol over Cobalt Catalysts. *Angew. Chem. Int. Ed.* **2018**, *57*, 6104–6108.
(24) Ouyang, B.; Xiong, S.; Zhang, Y.; Liu, B.; Li, J. The Study of Morphology Effect of Pt/Co_3O_4 Catalysts for Higher Alcohol Synthesis from CO_2 Hydrogenation. *Appl. Catal. A* **2017**, *543*, 189–195.
(25) Gogate, M. R.; Davis, R. J. Comparative Study of CO and CO_2 Hydrogenation over Supported Rh–Fe Catalysts. *Catal. Commun.* **2010**, *11*, 901–906.
(26) Caparrós, F. J.; Soler, L.; Rossell, M. D.; Angurell, I.; Piccolo, L.; Rossell, O.; Llorca, J. Remarkable Carbon Dioxide Hydrogenation to Ethanol on a Palladium/Iron Oxide Single-Atom Catalyst. *ChemCatChem* **2018**, *10*, 2365–2369.
(27) Nieskens, D. L. S.; Ferrari, D.; Liu, Y.; Kolonko, R. The Conversion of Carbon Dioxide and Hydrogen into Methanol and Higher Alcohols. *Catal. Commun.* **2011**, *14*, 111–113.
(28) Liu, S.; Zhou, H.; Zhang, L.; Ma, Z.; Wang, Y. Activated Carbon-Supported Mo–Co–K Sulfide Catalysts for Synthesizing Higher Alcohols from CO_2. *Chem. Eng. Technol.* **2019**, 42, 962–970.
(29) Wang, D.; Bi, Q.; Yin, G.; Zhao, W.; Huang, F.; Xie, X.; Jiang, M. Direct Synthesis of Ethanol via CO_2 Hydrogenation Using Supported Gold Catalysts. *Chem. Commun.* **2016**, *52*, 14226–14229.
(30) Wang, D.; Bi, Q.; Yin, G.; Wang, P.; Huang, F.; Xie, X.; Jiang, M. *Catal. Lett.* **2018**, *148*, 11–22.
(31) Murzin, D. Y.; Salmi, T. Catalytic Kinetics. *Chemistry and Engineering* **2016**, *chapter 3*, 101–152.
(32) Murzin, D. Y.; Salmi, T. Catalytic Kinetics. *Chemistry and Engineering* **2016**, *chapter 7*, 345–466.
(33) Chien, J. Y. Kinetic Analysis of Irreversible Consecutive Reactions. *J. Am. Chem. Soc.* **1948**, *70*, 2256–2261.